Geophysical Journal International

Geophys. J. Int. (2023) **234,** 2411–2428
Advance Access publication 2023 June 19
GJI Geodynamics and Tectonics

https://doi.org/10.1093/gji/ggad243

Characterizing the porosity structure and gas hydrate distribution at the southern Hikurangi Margin, New Zealand from offshore electromagnetic data

Christine Chesley [1], Samer Naif [2] and Kerry Key [3,*]

[1] *Department of Geology and Geophysics, Woods Hole Oceanographic Institution, Woods Hole, MA* 02543*, USA. E-mail: christine.chesley@whoi.edu*
[2] *School of Earth and Atmospheric Sciences, Georgia Institute of Technology, Atlanta, GA* 30332*, USA*
[3] *Department of Earth and Environmental Sciences, Lamont-Doherty Earth Observatory, Columbia University, Palisades, NY* 10964-1000*, USA*

Accepted 2023 June 14. Received 2023 May 26; in original form 2022 November 14

SUMMARY

The dynamics of accretionary prisms and the processes that take place along subduction interfaces are controlled, in part, by the porosity and fluid overpressure of both the forearc wedge and the sediments transported to the system by the subducting plate. The Hikurangi Margin, located offshore the North Island of New Zealand, is a particularly relevant area to investigate the interplay between the consolidation state of incoming plate sediments, dewatering and fluid flow in the accretionary wedge and observed geodetic coupling and megathrust slip behaviour along the plate interface. In its short geographic extent, the margin hosts a diversity of properties that impact subduction processes and that transition from north to south. Its southernmost limit is characterized by frontal accretion, thick sediment subduction, the absence of seafloor roughness, strong interseismic coupling and deep slow slip events. Here we use seafloor magnetotelluric (MT) and controlled-source electromagnetic (CSEM) data collected along a profile through the southern Hikurangi Margin to image the electrical resistivity of the forearc and incoming plate. Resistive anomalies in the shallow forearc likely indicate the presence of gas hydrates, and we relate deeper forerarc resistors to thrust faulting imaged in colocated seismic reflection data. Because MT and CSEM data are highly sensitive to fluid phases in the pore spaces of seafloor sediments and oceanic crust, we convert resistivity to porosity to obtain a representation of fluid distribution along the profile. We show that porosity predicted by the resistivity data can be well fit by an exponential sediment compaction model. By removing this compaction trend from the porosity model, we are able to evaluate the second-order, lateral changes in porosity, an approach that can be applied to EM data sets from other sedimentary basins. Using this porosity anomaly model, we examine the consolidation state of the incoming plate and accretionary wedge sediments. A decrease in porosity observed in the sediments approaching the trench suggests that a protothrust zone is developing ∼25 km seaward of the frontal thrust. Our data also imply that sediments deeper in the accretionary wedge are slightly underconsolidated, which may indicate incomplete drainage and elevated fluid overpressures of the deep wedge.

Key words: Permeability and porosity; Controlled source electromagnetics (CSEM); Magnetotellurics; Gas and hydrate systems; Subduction zone processes.

1 INTRODUCTION

Accretionary wedge complexes develop along convergent margins through the tectonic deformation of off-scraped and underthrusted sediments transported atop a subducting oceanic plate. These accretionary wedges cycle large volumes of water from the plate back to the ocean through the consolidation of pore spaces in sediments and crust and by dehydration reactions that release mineral-bound water from altered oceanic lithosphere. Constraining the volatile budget and extent of dewatering that occurs at these margins is relevant for characterizing the hydrogeology of accretionary wedges.

*Now at: BlueGreen Geophysics, LLC.

Additionally, because consolidation and dehydration reactions alter the mechanical properties of sediments, knowledge of the rate and distribution of dewatering is useful for determining the history and evolution of a wedge's internal structure. Thus, quantifying the input porosity and loss thereof for the crust and sediments within the accretionary wedge is crucial for calculating mass flux at subduction zones and for modelling the mechanical response of these deforming wedges (Bray & Karig 1985; Bekins & Dreiss 1992).

In addition to the role they play in the global water cycle, accretionary margins often provide a pressure and temperature environment that is ideal for the formation of gas hydrates, ice-like structures consisting of natural gas trapped in a solid lattice of water (Mienert 2022). Understanding the distribution of gas hydrate is important for several reasons. Much of the world's methane is bound in gas hydrate, which is why hydrate reservoirs are sinks for the global carbon cycle and potential energy resources (Crutchley *et al.* 2018). Because of the narrow pressure–temperature range in which solid hydrate is stable, gas hydrates have the potential to rapidly decompose in response to increasing ocean temperatures and pose both a climate hazard due to the release of methane and a geohazard related to triggering of landslides.

Flow of water and gas through the accretionary wedge is strongly controlled by the porosity and permeability of the host rock. These inextricably interrelated quantities not only regulate fluid flow but also alter effective stress along fault planes by modulating pore pressure, which may ultimately be linked to the occurrence and nature of megathrust slip (Bray & Karig 1985; Moore & Vrolijk 1992; Saffer & Bekins 2006; Saffer & Tobin 2011; Saffer & Wallace 2015; Warren-Smith *et al.* 2019). Because fluid flow influences effective stress and pore pressure in an accreting margin, it will also impact the structural development of the wedge and help determine whether landward- or seaward-vergent thrust faults form (Seely 1977; Tobin *et al.* 1993). Of particular importance for accretionary wedge growth is analysis of dewatering in the region immediately seaward of the main frontal thrust as this pertains to the development of the protothrust zone, the location of the next frontal thrust, and the spacing of consecutive imbricate thrust faults (Wang *et al.* 1994; Ito & Moore 2021). Moreover, estimating the amount of fluids input at the deformation front and released through various permeable pathways within the wedge and along the décollement remains a crucial component in accurately determining where sufficient overpressure exists to influence slip and to estimate the amount of water that is recycled at subduction zones.

Here we analyse electromagnetic data that span the incoming plate and accretionary wedge along the southern Hikurangi Margin, New Zealand. The resistivity models generated allow us to estimate the porosity of sedimentary units on the incoming plate and forearc in this region and highlight the abundance of gas hydrate and/or free gas present in this accretionary margin. Through removal of a background, compaction-based porosity model, we infer pore pressure conditions in the input sediments and accretionary wedge. We also show that the incoming plate sediments become increasingly dewatered as they approach the deformation front, suggesting the incipient formation of a protothrust zone can be imaged using electromagnetic techniques.

1.1 Hikurangi margin tectonic setting

The Hikurangi subduction zone, located offshore the North Island of New Zealand, formed through oblique subduction of the Pacific Plate beneath the Australian Plate (Fig. 1). Westward subduction of the Pacific Plate began *ca*. 27 Ma (Davy *et al.* 2008; Jiao *et al.* 2014) after a brief phase of southward subduction beneath the Chatham Rise from *ca*. 105 to 100 Ma (Davy *et al.* 2008; Hoernle *et al.* 2010; Davy 2014). Geodetic observations show a marked decrease in convergence rate from ∼60 mm yr^{-1} in the northernmost part of the margin to ∼20 mm yr^{-1} at its southernmost limit due to clockwise block rotation of the eastern North Island relative to the Australian Plate (Wallace *et al.* 2004). Moving southward, oblique subduction at the Hikurangi Margin eventually gives way to an entirely strike-slip accommodated relative plate motion in the Marlborough Fault System of New Zealand's South Island (Wallace *et al.* 2004) and then again becomes subduction in the reverse sense with the Australian Plate subducting beneath the Pacific Plate at the incipient Puysegur Trench (Gurnis *et al.* 2019).

In this area, the Pacific Plate is thickened relative to normal oceanic lithosphere by the Hikurangi Plateau, a Cretaceous Large Igneous Province (Davy *et al.* 2008). Geophysical estimates of the crustal thickness of the Hikurangi Plateau range from 9 km (Gase *et al.* 2021) to 35 km (Reyners 2013). Despite the large differences in these estimates, the plateau is at least 50 per cent thicker than normal ocean crust. IODP cores have sampled volcaniclastic lithologies at the top of the plateau, and subparallel reflectors in seismic data suggest that this layer of volcanics interbedded with sediment is 2–3 km thick in the northern part of the Margin (Barnes *et al.* 2020; Gase *et al.* 2021). It is evident that subduction of the buoyant Hikurangi Plateau has caused uplift in the eastern North Island and has led to a shallower forearc than is common at subduction zones, facilitating its extensive instrumentation (Litchfield *et al.* 2007; Wallace 2020). Compared to the much deeper (>9 km water depth) Kermadec trench to the north, the Hikurangi Margin is characterized by a shallow trench (∼3 km water depth; Barnes *et al.* 2010).

The Hikurangi Margin offers a natural laboratory in which to study dramatically varying megathrust behaviour in a relatively small geographic area. Of particular note in recent decades are intriguing along-strike variations in interseismic coupling and the occurrence of slow slip events (SSEs) at this subduction zone. With enhanced geodetic capabilities, including the widespread installation of campaign and continuous GPS sites, observations have revealed that the downdip limit of interseismic coupling transitions around Cape Turnagain from a depth of ∼40 km at the southernmost part of the margin to depths less than 15 km in the central and northern Hikurangi Margin (Fig. 1; Wallace *et al.* 2004). Additionally, the unitless coupling coefficient, ϕ_{ic}, which relates long-term fault slip to short-term creep rate, increases from $\phi_{ic} = 0.1$ to 0.2 in the northern Raukumara Peninsula and Hawke's Bay regions to $\phi_{ic} = 0.8$ to 1.0 in the south, suggesting that the southern part of the margin is more strongly seismically coupled than the northern margin (Wallace *et al.* 2004). Because these large coupling coefficients occur over a broad region of the southern North Island (90–180 km wide and ∼40 km deep), large subduction earthquakes with magnitudes of M_w 8.2–8.7 may be possible and thus present a serious potential seismogenic hazard for New Zealand (Wallace *et al.* 2009; Clark *et al.* 2015).

At the southern end of the Hikurangi Margin, the incoming plate is covered by a thick section of sediment that thins to the north, exposing numerous seamounts. Differences in the roughness of the Pacific Plate are notable in bathymetric maps of the region (Figs 1 and 2). Some have proposed that this subducting topography may prevent the build-up of large stresses and thus promote creeping in the northern Hikurangi Margin (Wallace *et al.* 2009; Bell *et al.* 2010; Chesley *et al.* 2021). Seismotectonic analogue models show that rougher plate interfaces lead to weaker interseismic coupling

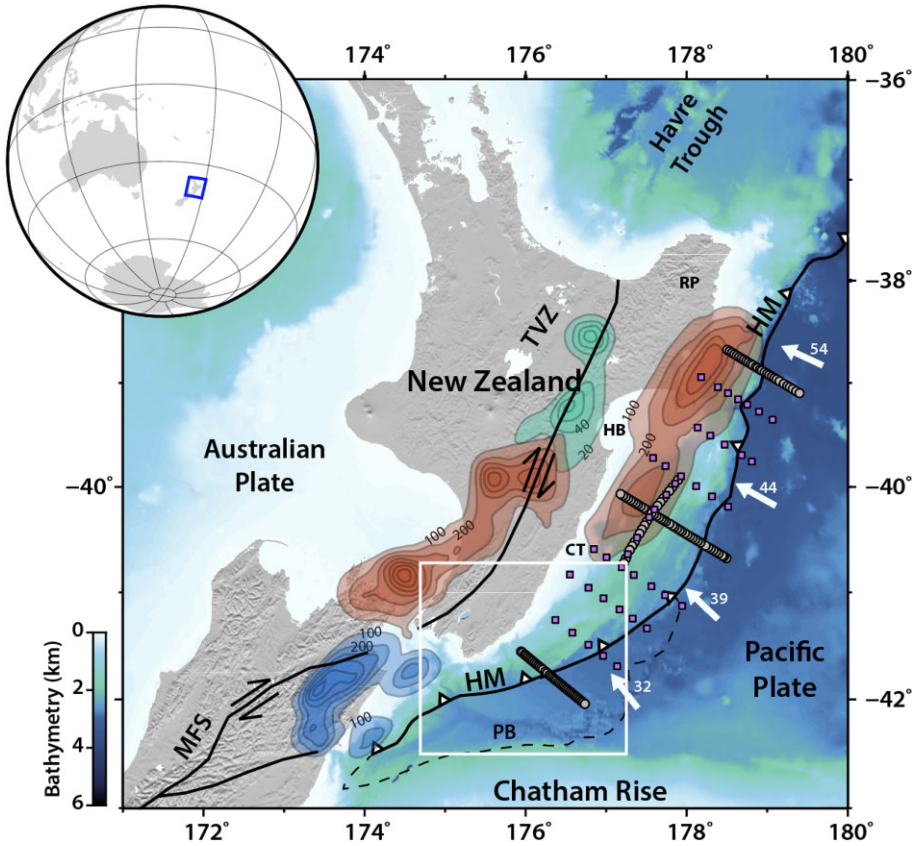

Figure 1. Tectonic setting of the Hikurangi Margin. Grey circles are locations where controlled-source electromagnetic data and magnetotelluric (MT) data were collected during the Hikurangi Trench Regional Electromagnetic Survey to Image the Subduction Thrust described in Section 2. Purple squares are locations where long-period MT data were collected. White arrows indicate convergence rate and direction of the Pacific Plate relative to the Australian Plate in mm yr^{-1}. Shaded contours are cumulative slip patches in 100 mm (red and blue) or 20 mm (green) contour intervals from slow slip events (SSEs): Red—SSEs from 2002 to 2014; Green—deep slip associated with 2006 and 2008 SSE and Blue—afterslip from 2016 Kaikoura earthquake [see ref. Wallace (2020) and refs therein]. Dashed black curve outlines the Pegasus Basin. HM, Hikurangi Margin; TVZ, Taupo Volcanic Zone; RP, Raukumara Peninsula; HB, Hawke's Bay; CT, Cape Turnagain; PB, Pegasus Basin and MFS, Marlborough Fault System. The white box is an outline of the region shown in Fig. 2, which is the focus of this paper.

than their smooth counterparts by producing a more heterogeneous stress distribution along the megathrust (van Rijsingen *et al.* 2019). This, in turn, partitions the interface and results in lower integrated fault strength than can be achieved along smoother interfaces (Dominguez *et al.* 1998, 2000; van Rijsingen *et al.* 2019). Global subduction zone compilations support these modelling efforts and find a statistically significant relationship between the thickness of subducting sediment and the magnitude of megathrust events, with earthquakes $M_w \geq 7.5$ being more likely to nucleate where thicker subducting sediment packages ($\geq$1 km) are present (Scholl *et al.* 2015). Recent geophysical investigations at the northern Hikurangi Margin have revealed the presence of a subducting seamount and associated upper plate damage zone in a region that experienced slip during the 2014 SSE (Bell *et al.* 2010; Wallace *et al.* 2016; Barker *et al.* 2018; Chesley *et al.* 2021). Although the exact relationship between this subducted topography and the 2014 SSE is unclear, Chesley *et al.* (2021) observed large variations in fluid content along the plate interface, which is consistent with the substantial lithological heterogeneity imaged seismically (Barnes *et al.* 2020). They suggest that the seamount played a role in modulating vertical fluid release from the slab, thus contributing to the cyclic nature of slow earthquake occurrence (Warren-Smith *et al.* 2019). Observations of increasing sediment subduction from the shallow SSE regime of the north to the locked zone in the southern Hikurangi Margin as well as a change in the lithology of the megathrust-hosting protolith from volcaniclastics interspersed with calcareous pelagic sediments to siliciclastic sediments have also been implicated in controlling the slip transition (Gase *et al.* 2022)

Sediment thickness increases from ~1 km off the Raukumara Peninsula in the north to >5 km in the southernmost part of the margin due to increasing proximity to submarine canyons in the south that supply turbidites to the trough (Barnes *et al.* 2010). The imbricated frontal accretionary wedge that is actively being built landward of the trench ranges from 10 to 200 km in width (Barker *et al.* 2009) and is compositionally divided into three major sections: (1) inner Late Cretaceous and Palaeogene rocks that preceded subduction, (2) outer wedge accreted trench-fill turbidites, which are late Cenozoic in age and correlate with sequences found in the Hikurangi Trough on the incoming plate and (3) a Miocene–present deforming cover sequence of shelf and slope sediments (Barnes *et al.* 2010). The ubiquity of bottom-simulating reflectors (BSRs) in seismic reflection data point to the prevalence of free gas and/or gas hydrates in both the accretionary wedge and Hikurangi Trough (Barnes *et al.* 2010; Plaza-Faverola *et al.* 2012; Crutchley *et al.* 2015; Fraser *et al.* 2016; Wang *et al.* 2017; Crutchley *et al.* 2018; Han *et al.* 2021; Kroeger *et al.* 2022).

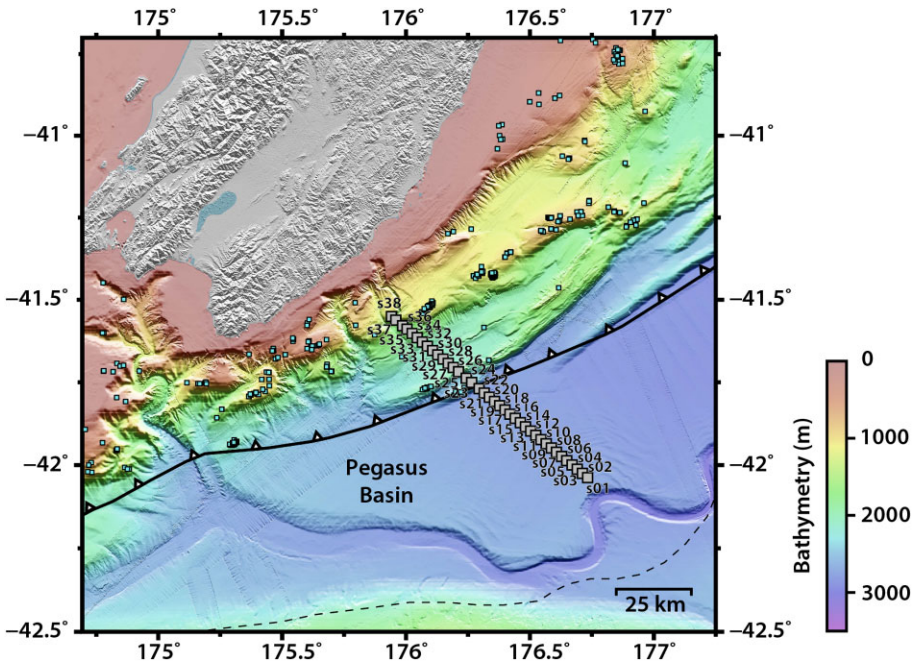

Figure 2. Bathymetric map for the area of the southern Hikurangi Margin discussed here (white rectangle in Fig. 1). Bathymetry data are from Ryan *et al.* (2009). Grey squares are locations of the OBEMs. Light blue squares are locations where evidence for fluid seeps exists (Watson *et al.* 2020).

2 HT-RESIST DATA COLLECTION AND PROCESSING

We carried out the Hikurangi Trench Regional Electromagnetic Survey to Image the Subduction Thrust (HT-RESIST) from December 2018 to February 2019. Data acquisition was completed aboard the R/V Roger Revelle and involved simultaneous collection of controlled-source electromagnetic (CSEM) data and magnetotelluric (MT) data at a total of 136 stations using a fleet of 42 ocean bottom electromagnetometers (OBEMs). We used the Scripps Institution of Oceanography Mk III broadband OBEMs with 10 m long electric dipoles and induction coil magnetometers capable of measuring orthogonal, horizontal electric and magnetic field components in the 0.0001–500 Hz frequency band (Constable 2013). We used a 125 Hz sampling rate and the broadband recording capacity allowed for the simultaneous collection of high frequency (0.1–10 Hz) CSEM and longer-period (0.0001–0.1 Hz) MT data.

Our complete survey (Fig. 1) included three trench-crossing profiles that spanned the north–south extent of the Hikurangi Margin and one approximately trench-parallel profile that crossed the transition from weak to strong interseismic coupling (Wallace *et al.* 2004, 2009). After gathering the data from these profiles, we additionally deployed an array of 42 OBEMs, which collected long-period MT data for approximately six weeks. Here, we discuss results from the southernmost trench-crossing profile, the data for which we collected over the course of 5 d (Fig. S1). Results for the northernmost profile are presented in Chesley *et al.* (2021).

2.1 Magnetotelluric data

The magnetotelluric (MT) method capitalizes on natural time variations in Earth's magnetic field as its source for electromagnetic induction. The time-varying source currents that originate in the ionosphere are generated by the interaction of Earth's magnetic field with the solar wind, creating a low frequency electromagnetic signal that diffuses down through the seafloor, where its amplitude and phase are modified in a manner that is controlled by the underlying resistivity (Chave & Weidelt 2012). Our OBEMs recorded these electric and magnetic field variations throughout the five day deployment period (Fig. S1).

In processing the MT data, we seek to accurately estimate the impedance tensor at each frequency of interest from the electric and magnetic field time-series and to assign statistical uncertainty to each of these impedance tensor estimates. The impedance tensor is the Earth response function that relates variations in the horizontal electric and magnetic fields:

$$\mathbf{E} = \mathbf{ZH} \tag{1}$$

$$\mathbf{Z} = \begin{bmatrix} Z_{xx} & Z_{xy} \\ Z_{yx} & Z_{yy} \end{bmatrix}, \tag{2}$$

where **E** and **H** are the frequency dependent electric and magnetic fields, respectively, and **Z** is the complex-valued, frequency-dependent impedance tensor. Note that the x and y subscripts refer to any two arbitrary orthogonal directions in the horizontal plane.

We apply the robust remote reference multistation processing approach of Egbert (1997) to estimate **Z**. Using a multiple station approach to impedance tensor estimation is advantageous because it increases the attainable signal-to-noise ratio (SNR) and is less sensitive to outliers in remote stations compared to single station remote reference schemes (Egbert 1997). With this method, the electric and magnetic field time-series data are first Fourier transformed to the frequency domain using pre-whitened, overlapping windows of data and cascade decimation, which optimizes computations by reducing the number of time samples required in the Fourier transforms for the lowest frequencies of interest. Instrument channel-specific, frequency-dependent calibrations are applied to each electric and magnetic field channel to remove the sensor and amplifier responses. The amplitudes of the resulting Fourier coefficients obtained are manually inspected as spectrograms to remove any data before the instrument settles on the seafloor and after it is released to return to the surface; to flag dead or poorly connected

channels; and to remove data recorded during CSEM tows. After obtaining the impedance estimates, we inspected them for 2-D compatibility and removed all data that suggested the presence of 3-D induction effects, as indicated by the shape of the impedance polarization diagram, or by Swift skew (S_s) values $\geq$0.26 (Swift 1967), where

$$S_s = \frac{|Z_{xx} + Z_{yy}|}{|Z_{xy} - Z_{yx}|} \quad . \tag{3}$$

Such 3-D distortions tended to appear at periods >300 s (Fig. 3). We noted that receiver s38 showed a stark rotation in strike at periods $\geq$100 s compared to the other receivers in the survey and chose not to include its data in the inversion. Of the 38 receivers deployed on this profile, we modelled the MT data from 32 of them.

2.2 Controlled-source electromagnetic data

CSEM data were collected by deep-towing the Scripps Underwater Electromagnetic Source Instrument (SUESI) approximately 100 m above the seafloor to minimize signal attenuation through seawater and maximize signal coupling to the crust, while also maintaining a safe towing altitude above bathymetric features (Constable 2013). For this survey, SUESI output a 230–310 A alternating current across a 300 m horizontal electric dipole terminated by copper electrodes. This alternating current induces electric and magnetic fields that propagate through the underlying lithosphere and are attenuated based on its resistivity. We used the complex binary Waveform D of Myer *et al.* (2011) with a fundamental transmission period of 4 s. Waveform D is doubly symmetric and designed to spread the high power harmonics over about a decade of frequency, thus allowing for constraints on the resistivity structure at different length scales (Myer *et al.* 2011).

We employed the inverted long-baseline (ILBL) system described in Key & Constable (2021) to navigate SUESI's position and orientation in the water column. We expect that the ILBL system provides accuracy to within 5 and 37 m in the inline and crossline positions, respectively (Key & Constable 2021), and that the pressure sensor used can measure SUESI's depth to an accuracy better than 1 m.

To estimate the locations of our OBEMs, we used a long-baseline (LBL) navigation system, which exploits two-way traveltimes (TWTTs) between the ship and OBEMs to triangulate the OBEMs' positions. We use TWTTs along with the ship's GPS location and a seawater velocity-depth profile based on SUESI's CTD unit in a Levenberg-Marquardt inversion for the OBEM's location, similar to the procedure used to navigate ocean-bottom seismometers (Russell *et al.* 2019). In addition to estimating the OBEM location on the seafloor, our processing workflow uses linearized uncertainty analysis to estimate the uncertainty in the navigated position. This method allowed for the determination of OBEM locations to within 11 m for all receivers and a median of 3.7 m.

We processed the CSEM time-series data by dividing the time-series into 4 s windows, the length of the fundamental period. These sections were then pre-whitened, Fourier transformed, and post-darkened to produce Fourier coefficients (Myer *et al.* 2011). The Fourier coefficients were normalized by the complex source dipole moment and corrected for the individual sensor responses of each OBEM. To reduce variance, the Fourier coefficients were then stacked in 240 s segments using an algorithm that iteratively removes any outliers present. Because the seafloor sediment package is so thick in the southern Hikurangi Margin, the CSEM data are sensitive to a predominantly laterally invariant 1-D resistivity structure. Hence this longer than typical stack time allowed for

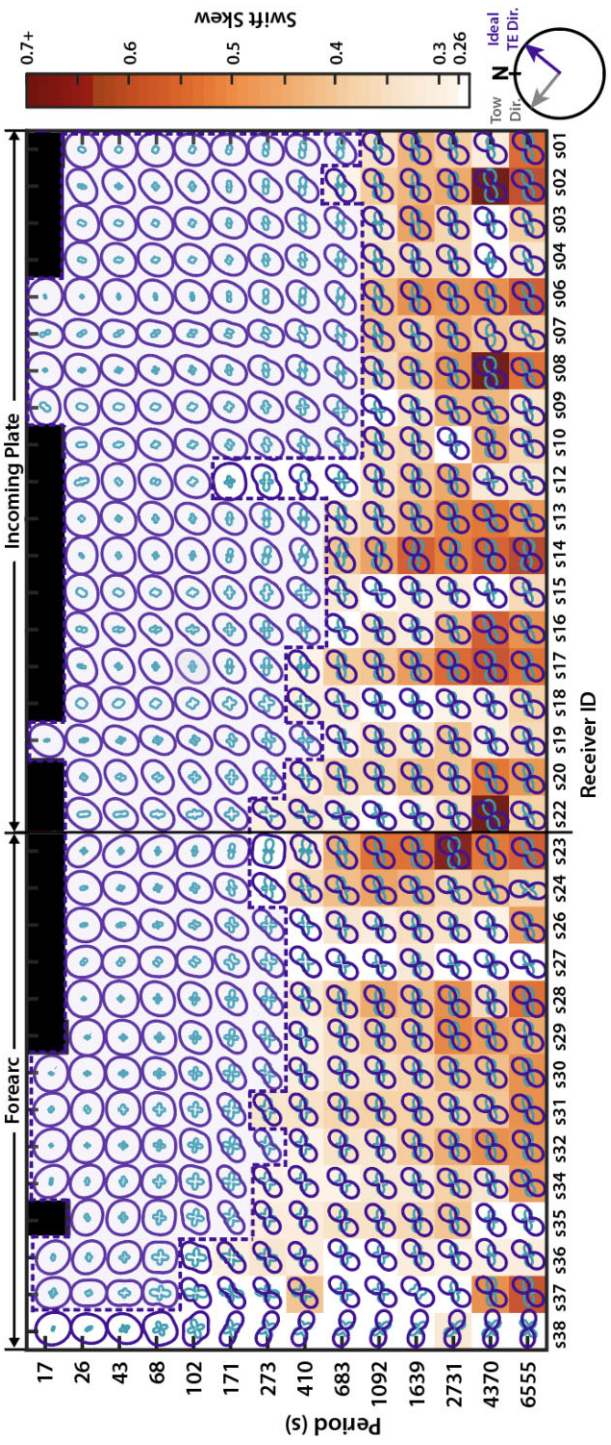

Figure 3. MT impedance polar diagrams with Swift skews for all of the Southern HT-RESIST data. $|Z_{xy}|$ and $|Z_{xx}|$ are dark and light blue, respectively. Swift skews below the 0.26 cut-off are white or light blue. Skews above this cut-off are shaded orange. Periods where the MT response curve deviates from varying smoothly are blacked out. Data used in the inversion are indicated by light blue shading and dashed blue boxes. The compass rose shows the direction of the CSEM tow path (grey) and the direction oblong impedance polar diagrams should ideally point (dark blue) in order to be compatible with the 2-D modelling performed here.

data reduction without loss of lateral structural resolution. The variance of each stack, and hence the data error, was assigned based on the stack residuals. The instrument sensor error floors are used to calculate the SNR of the stacked data. We discarded data with SNRs less than or equal to 2 because such noisy data offer little information and can contaminate the model by allowing for a much wider range of model parameters. We then manually removed any outliers that remained afterwards. Receivers s05, s11 and s25 experienced poor electrode connections on the electric field channels, and therefore the electric field data from those receivers were unusable. The SUESI tow path deviated severely from the inline direction over receivers s07, s36, s37 and s38, so we did not include the CSEM data from those receivers in our analysis. Technical errors in downloading the data caused us to lose the data from receiver s33. We, therefore, modelled the CSEM data from the 30 remaining OBEMs.

3 CSEM AND MT DATA INVERSION

We used the MARE2DEM code to jointly invert the CSEM and MT data. MARE2DEM is a freely available, parallel, adaptive finite element code that, among its other capabilities, can perform nonlinear, regularized, anisotropic joint inversion of marine CSEM and MT data. Because the EM inversion problem is ill-posed, we use regularization in the form of a model roughness norm to stabilize the solution (Constable *et al.* 1987). In MARE2DEM, the inversion seeks to minimize the functional (Key 2016):

$$U = \lambda^{-1}||\mathbf{W}(\mathbf{d} - \mathcal{F}(\mathbf{m}))||^2 + ||\mathbf{Rm}||^2, \quad (4)$$

where $\mathbf{d}$ is the data vector, $\mathcal{F}(\mathbf{m})$ is the forward response for model parameters, $\mathbf{m}$, $\mathbf{W}$ is a diagonal matrix of inverse standard errors on the data, and $||\mathbf{W}(\mathbf{d} - \mathcal{F}(\mathbf{m}))||^2$ is the model misfit term. $\mathbf{R}$ is the model roughness operator and the Lagrange multiplier term, λ, defines the relative weight placed on minimizing the model roughness compared to the weight placed on minimizing the model misfit. Conceptually, increasing the penalty against model roughness (increasing λ in eq. 4) steers the inversion away from models that contain sharp resistivity gradients between adjacent grid cells and thus forces resistivity to vary smoothly with depth and lateral distance in the Earth. This assumption is not unreasonable given that the dominant control on shallow lithospheric resistivity in the marine setting is porosity, a property that typically decreases exponentially with depth (Bahr *et al.* 2001). Such a penalty does not preclude the inversion from finding rougher models but rather drives the inversion away from such models unless the data require dramatic resistivity contrasts.

Early isotropic inversions of the HT-RESIST data indicated the presence of anisotropy in the seafloor sediments consistent with horizontally layered isotropic sedimentary sequences (e.g. Newman *et al.* 2010; Du & Key 2018). We therefore inverted the data for vertical transverse isotropy in which the horizontal components of resistivity comprise a plane of isotropy and the resistivity tensor has the form:

$$\bar{\bar{\rho}} = \begin{bmatrix} \rho_h & & \\ & \rho_h & \\ & & \rho_v \end{bmatrix}, \quad (5)$$

where ρ_h and ρ_v are the horizontal and vertical resistivity, respectively (see Fig. S2 for model anisotropy ratios).

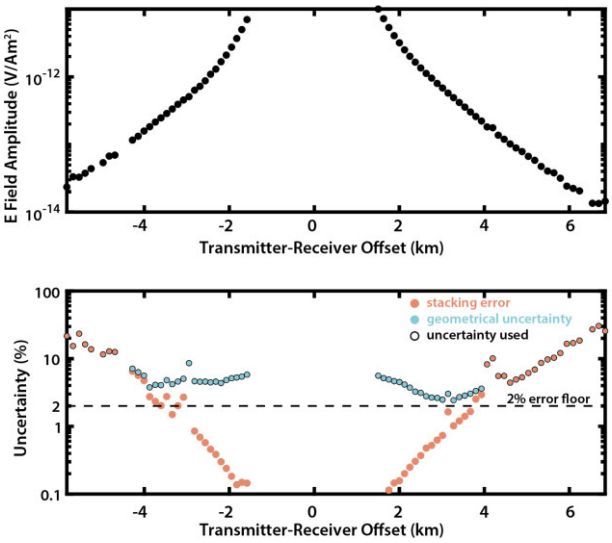

Figure 4. (a) Inline electric field amplitude for receiver s10 at 0.25 Hz and (b) uncertainty for these data. In (b), light blue and red circles are the geometrical uncertainty and true stacking errors, respectively. Uncertainty values outlined in black indicate the error structure used when modelling the data. The dashed black line shows where a 2 per cent error floor would lie. At short transmitter-receiver offsets, the geometrical uncertainty increases with decreasing offset because of the impact of navigational uncertainties, whereas the uncertainty increases at larger offsets due to the absolute noise floor of the electric field.

3.1 Estimating geometric uncertainty

Navigational uncertainties will impact the error in CSEM data to varying degrees depending on the relative transmitter-receiver geometry. Importantly, shorter offset data will be more affected by inaccuracies in navigation estimates than longer offset data due to the manner in which EM field amplitudes decay—the amplitude changes rapidly when the source is nearby, and more gradually with increasing transmitter–receiver distance (see Fig. 4a). The navigational parameter with the most potential to impact uncertainty in the data is the relative transmitter–receiver separation, but uncertainties in the transmitter dip and azimuth will compound the effects of geometrical uncertainties as well. In order to appropriately model the data and avoid overfitting sources of navigational noise, we apply the method of (Myer *et al.* 2012), which uses uncertainty in the navigational parameters to estimate a composite geometrical uncertainty on each CSEM data point. Often, this 'geometrical uncertainty' is greater than the 2 per cent error floor at short offsets (Fig 4); at longer offsets, the stacking errors dominate.

3.2 Resistivity models of the southern Hikurangi Margin

The southern HT-RESIST profile crosses the Hikurangi Margin in a region devoid of shallow SSEs and where significant seafloor topography on the incoming plate is absent (Fig. 2). The smoothness of the incoming plate bathymetry indicates thick sediments fill the Pegasus Basin. To highlight the complementary sensitivities of CSEM and MT data, we show inversions using each data type along with the preferred joint CSEM-MT inversion model. Unless otherwise stated, the starting model for all inversions is a uniform, 1 Ω-m half-space.

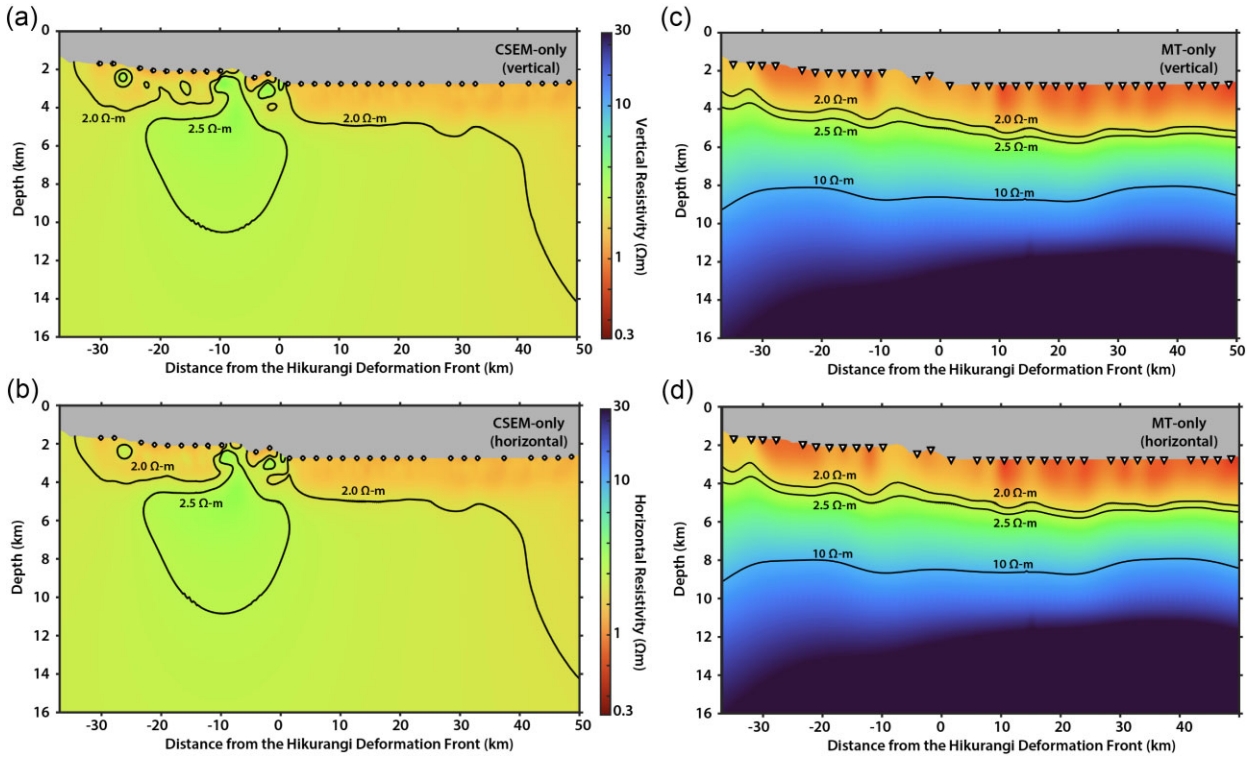

Figure 5. Individual inversions of the (a)–(b) CSEM and (c)–(d) MT data at the southern Hikurangi Margin. Resistivity contours of 2, 2.5 and 10 Ω-m are shown for clarity. Each inversion is for vertical transverse isotropy with (a) and (c) being the vertical components of the resistivity model and (b) and (d) being the horizontal components. White circles in (a)–(b) are receivers with usable CSEM data. Inverted white triangles in (c)–(d) are receivers with usable MT data.

3.2.1 CSEM-only inversion

We inverted the three highest power frequencies (0.25 Hz, 0.75 Hz, and 1.75 Hz) of the CSEM data using the geometrical uncertainty and 2 per cent error floor described in Section 3.1 (Figs 5a and b). The model converged to RMS = 0.995. This inversion model confirms that conductive sediments blanket the incoming plate and forearc in at least the upper 2 km of the profile. Because of this considerable sediment thickness, the controlled-source signal attenuates rapidly with depth and the CSEM data have limited sensitivity to structure beneath the sediments. The model does suggest an increase in resistivity with depth beneath the sediments, but the details of that increase are masked by the thick conductive package that covers the seafloor.

Within the flat-lying forearc from −28 to −24 km and the two ridges just landward of the trench, resistors (1.8–3.5 Ω-m) appear to follow the seafloor bathymetry at depths of ∼200–700 m below seafloor (mbsf). Based on the prevalence of BSRs in this region (Plaza-Faverola *et al.* 2012; Crutchley *et al.* 2015, 2018, 2020; Fraser *et al.* 2016; Koch *et al.* 2016; Turco *et al.* 2020; Han *et al.* 2021; Kroeger *et al.* 2022), it seems likely that these resistors indicate the presence of gas hydrates and/or free gas, and we note that these resistors are similar to resistive hydrates and gas seen in EM results from surveys at other continental margin locations (Hyndman *et al.* 1999; Constable 2010; Weitemeyer *et al.* 2011; Myer *et al.* 2015; Attias *et al.* 2018). Some resistors appear beneath gaps in our receiver spacing, but we remind the reader that CSEM data are sensitive to seafloor structure between the receiver and transmitter, and not just beneath the receiver. This means that, even with the ≤5.7 km spaces between receivers, the CSEM data are still sensitive to shallow resistors. Indeed, these shallow resistors appear even in models where data from alternating receivers in the forearc are excluded from the inversion (Figs S3–S4. A diffuse, less resistive band appears to extend from −23 to −14 km, which might suggest that the flat-lying forearc resistor and ridge resistors are connected. Resistors beneath the second ridge at 3.2–5.6 km depth are most likely associated with localized dewatering along thrust faults and excess pore closure due to horizontal compression.

3.2.2 MT-only inversion

We inverted the 2-D compatible MT data shown in Fig. 3 with periods ranging from 17 to 683 s and an error floor of 8 per cent to avoid overfitting and to allow for a balance between the MT and CSEM data fits (Figs 5c and d); the model converged to RMS = 1.009. These longer periods allow for greater depth sensitivity compared to the CSEM data, and so the MT-only inversion model illuminates the transition from conductive sediments to the top of the resistive Hikurangi Plateau, approximately consistent with the 10 Ω-m contour (Mochizuki *et al.* 2019). Because the 2-D compatible MT data periods are not long enough to show us the peak in apparent resistivity of the MT response, this value may underestimate the true resistivity. It is, however, consistent with the resistivity of volcaniclastic material (Naif *et al.* 2015; Chesley *et al.* 2019, 2021; Johansen *et al.* 2019), that characterizes the upper ∼1.5–3 km of the Hikurangi Plateau (Davy *et al.* 2008; Mochizuki *et al.* 2019; Gase *et al.* 2021). The uppermost sediments appear more conductive than they were in the CSEM-only

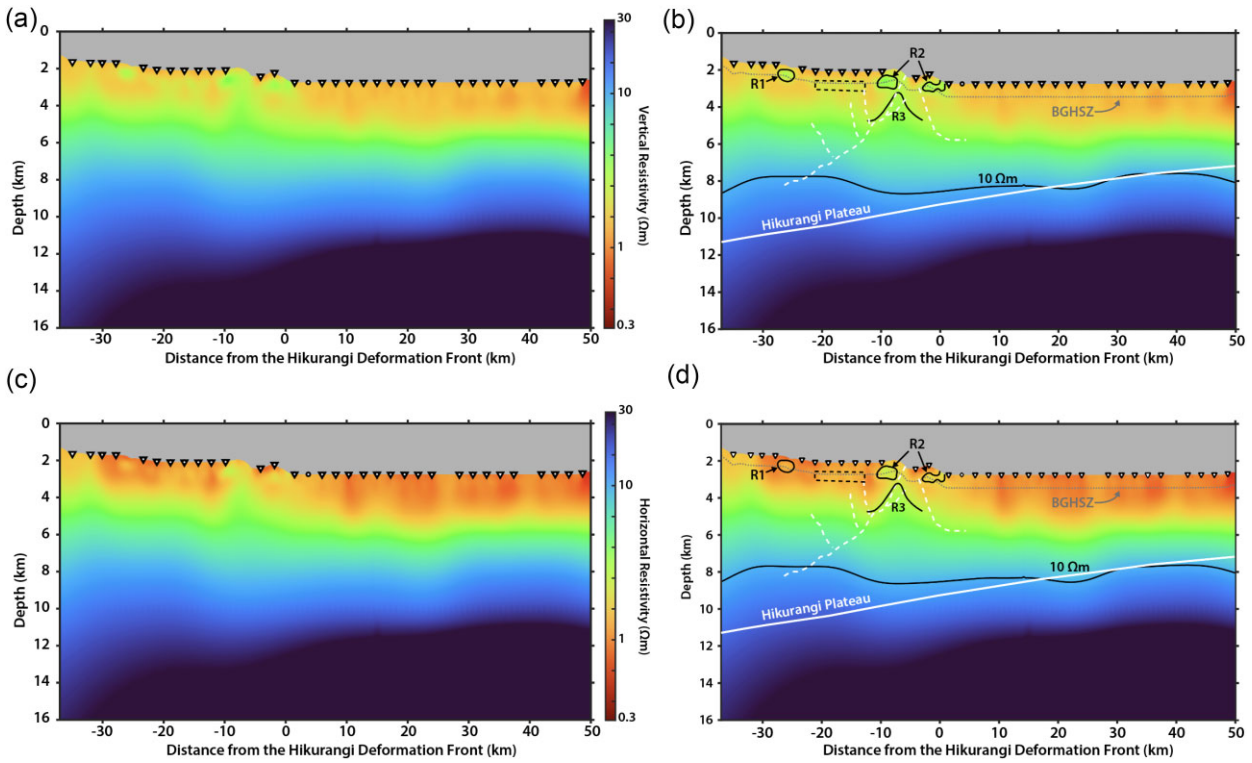

Figure 6. Joint vertical transverse isotropic inversion of the CSEM and MT data at the southern Hikurangi Margin with interpretations shown on the right. White circles are receivers with usable CSEM data and inverted white triangles are receivers with usable MT data. (a)–(b) Vertical resistivity and (c)–(d) horizontal resistivity. Black outlines in (b) and (d) are interpretations discussed in the text and the 10 Ω-m resistivity contour. The dashed grey line in (b) and (d) is the approximate depth of the base of the gas hydrate stability zone (BGHSZ). The white solid and dashed lines are the approximate depth to the top of the Hikurangi Plateau and the estimated locations of thrust faults, respectively, from the SAHKE-01 seismic reflection data and velocity models in Mochizuki *et al.* (2019).

inversion and there is no longer any evidence of forearc resistors. Both of these observations are related to the complementary aspects of CSEM and MT data. MT data are most sensitive to horizontal resistivity whereas inline CSEM data are primarily sensitive to resistivity variations within the vertical plane between the transmitter and the OBEM; broadside CSEM data have greater sensitivity to horizontal resistivity (Newman *et al.* 2010; Martí 2014; Key 2016). For layered seafloor sediments, resistivity should be lower in the horizontal plane because this plane corresponds to parallel (versus series) resistance. Therefore, the sediments appear to be more conductive in the MT-only inversion because the MT data are more sensitive to the parallel resistance of the layered sediments. Additionally, electrical currents are preferentially induced in conductors, which is why MT data are more sensitive to conductive rather than thin, resistive anomalies (Constable 2013). On the other hand, resistive layers give rise to slower data amplitude decay with transmitter-receiver offset and slower phase changes than do conductive regions, making CSEM data much more sensitive to thin resistors than MT data (Constable 2013). The lower-frequency MT data also have much less resolution to shallow structure relative to the higher-frequency CSEM data. Thus the forearc resistors appear in the CSEM-only inversion but not in the MT-only model.

3.2.3 *Joint CSEM and MT inversion*

The joint CSEM-MT inversion shows many of the features noted individually in the CSEM-only and MT-only inversions (Fig. 6). This model converged to RMS = 0.994; Figs S5–S12 give detailed breakdowns of the model fits.

A 5–6-km-thick package of sediments (0.8–10 Ω-m) covers the incoming plate. These sediments exhibit a gradual increase in resistivity until roughly 2.5 km below seafloor (kmbsf) where their resistivity begins to grow more rapidly. The Hikurangi Plateau is apparent as the dipping resistor beneath the sediments; we use the 10 Ω-m contour as the approximate top of the Plateau because it nearly matches the boundary for the plateau identified in Mochizuki *et al.* (2019), and because 10 Ω-m is a reasonable resistivity estimate for the volcanic material that covers the Plateau (Naif *et al.* 2015; Chesley *et al.* 2019; Johansen *et al.* 2019; Chesley *et al.* 2021). In the shallow forearc, resistors from −28 to −24 km (R1) and in the ridge (R2) again appear conspicuously along with the conical resistor beneath the landward-most ridge (R3).

As with the CSEM-only inversion, there seems to be a diffuse resistive layer from −23 to −14 km that may connect R1 and R2 (dashed black lines in Fig. 6). To assess the necessity of this resistive layer connection by the data, we fixed its resistivity to 1.5 and 1 Ω-m in the vertical and horizontal directions, respectively, which is similar to the resistivity of the surrounding sediment. We inverted the remaining model space (Figs S13a and b). Although this model converged with an acceptable RMS misfit of 1.001, the new model includes a halo of increased resistivity around the zone of fixed resistivity. This can be observed more clearly by examining the difference in resistivity between this new model and that of the preferred model (Figs S13c and d). This analysis suggests, therefore, that some form of resistive connection between R1 and R2 is required by the data.

4 DISCUSSION

4.1 Porosity of the southern Hikurangi Margin

Quantifying the porosity of sediments before they enter the trench and upon accretion or subduction is key to determining their consolidation state and understanding how deformation mechanisms and dewatering pathways operate in a given subduction system. This in turn has implications for the strength of the megathrust and its ability to nucleate earthquakes Marone & Scholz (1988).

The porosity of the outer forearc margin has generally been determined using cores from drilling expeditions and seismic velocity models, each of which has its limitations. Although they allow for *in situ* porosity measurements with high accuracy to be obtained, core samples are localized data points and extensive coring is resource prohibitive. Additionally, most cores penetrate less than the top 2 km of sediment and oceanic crust (International Ocean Discovery Program 2021). Seismic techniques, on the other hand, provide porosity estimates on a much broader scale spatially. Yet seismic waves are strongly influenced by lithology in addition to porosity, resulting in poorer accuracy of seismically derived porosity.

Because the electrical resistivity of sediments is strongly dependent on porosity (Naif *et al.* 2021), EM geophysical methods are the ideal candidate for providing porosity constraints over large swaths of seafloor. EM methods have been applied in a number of deep-water and continental shelf settings to map both the porosity and salinity of, for example, oceanic crust, incoming plate bending faults, seamounts, the outer forearc, and submarine aquifers (Evans 1994; Naif *et al.* 2015, 2016; Gustafson *et al.* 2019; Attias *et al.* 2020; Micallef *et al.* 2020; Chesley *et al.* 2021). For our applications at Hikurangi, it is relevant to note that saline fluids, namely seawater, are more conductive than most near-surface, rock-forming minerals by several orders of magnitude (Naif *et al.* 2021). This, importantly, means that the bulk resistivity of the forearc and Hikurangi Plateau are essentially controlled by their porosity and the resistivity of the pore fluid.

The strong dependence of resistivity on porosity in the shallow subsurface allows for the estimation of porosity from a resistivity model. One of the most widely used relationships between porosity and resistivity is the empirical Archie's law (Archie 1942):

$$\phi = \left(\frac{\rho_f}{\rho}\right)^{\frac{1}{m}}, \tag{6}$$

where ϕ is porosity, ρ is the bulk resistivity, ρ_f is the pore fluid resistivity and m is the cementation exponent. The shape of grains, which directly influences the shape of pore spaces, is one of the most important factors that determines the cementation exponent. Higher angularity of the grains translates to larger values of m (Salem & Chilingarian 1999). More intense fracturing will lead to lower m values. Lithology also influences m with higher contents of sand and fractured limestone corresponding to lower m values (Salem & Chilingarian 1999). Here we choose $m = 2.4$ as it is consistent with other studies in the southern Hikurangi Margin (Schwalenberg *et al.* 2017). Because our resistivity model suggests an anisotropic structure, the cementation exponent should realistically be represented by a tensor to allow pore geometry to vary with direction (Kennedy *et al.* 2001; Liu & Kitanidis 2013). We do not, however, have constraints on such directional dependence of the cementation factor and have instead chosen to use the geometric mean of the diagonal elements of the resistivity tensor in porosity calculations, that is: $\sqrt[3]{\rho_h\ \rho_h\ \rho_v}$ (Guo *et al.* 2022). We assume the pore fluid has seawater salinity and compute its temperature-dependent resistivity using the following relationship from Constable *et al.* (2009):

$$\rho_f^{-1} = 2.903916(1 + 0.0297175T + 1.5551 \times 10^{-4}T^2 - 6.7 \times 10^{-7}T^3), \tag{7}$$

where T is the seawater temperature in °C. We assumed a linear temperature profile:

$$T = T_0 + H\Delta z, \tag{8}$$

where T_0 is temperature at the seafloor found by extrapolating temperatures recorded by the CSEM transmitter; such values ranged from 1.2 to 5.3 °C. H is the geothermal gradient, which was estimated as 29 °C km^{-1} from modelling of BSRs in a seismic reflection profile near our study area (Fohrmann & Pecher 2012). Δz is depth below seafloor.

Due to surface-mediated ion transport conduction mechanisms, the presence of clay minerals in the subsurface can cause porosity estimates obtained from Archie's law to be higher than the true porosity of the crust and seafloor sediments (Pezard *et al.* 1989). A modified form of Archie's law may be applied to account for such surface conduction and takes the form (Sen & Goode 1992; Naif *et al.* 2016):

$$\phi = \left(\frac{\rho_f}{\rho(1+\rho_f R)}\right)^{\frac{1}{m}} = \left(\frac{\sigma}{\sigma_f + R}\right)^{\frac{1}{m}}, \tag{9}$$

$$R = 1.3\mu_T Q_v + \frac{1.93m\ \mu_T\ Q_v}{1 + 0.7\mu_T\ \rho_f}, \tag{10}$$

where σ is the electrical conductivity, which is the reciprocal of the electrical resistivity (ρ^{-1}), Q_v is the volumetric concentration of charges and μ_T is the mobility of counter-ions, which varies with temperature:

$$\mu_T = 1 + 0.0414(T - 22)\ . \tag{11}$$

The contribution of clay minerals to the bulk resistivity varies with Q_v, and increasing clay contents correspond to larger Q_v and m values. Examining the effect of temperature on the denominator of eq. (9) for $Q_v = 0.5$, a value that might be typical of smectite-rich sediments (Revil *et al.* 1998), shows that the modified Archie's denominator is approximately equal to the fluid conductivity when the fluid conductivity is greater than or approximately equal to that of seawater (Fig. S14). This difference is especially negligible at lower temperatures. Because seawater conductivity increases with temperature, the increases in R (and hence $R + \sigma_f$) with increasing temperature are nearly offset so that the Archie's denominator is still essentially equivalent to the conductivity of seawater. Deviations arising at higher temperatures are comparable to the uncertainty in the cementation exponent. For fresher systems, on the other hand, $R + \sigma_f$ diverges appreciably from σ_f such that surface conduction from clays is expected to be the dominant conduction mechanism (Sen & Goode 1992). It is reasonable to assume that the pore fluid within the seafloor sediments and crust at Hikurangi is seawater (or free gas in the case of the forearc anomalous resistors). Thus surface conduction from clays is negligible when compared to conduction from ion mobility in seawater, and its exclusion should not greatly impact porosity estimates.

The resistivity-derived porosity model for the Southern HT-RESIST data is shown in Fig. 7. For regions of the model where gas hydrate or free gas are likely present we instead show estimates of the hydrate saturation. This is discussed further in Section 4.3. As is expected, the first-order trend is a decrease in porosity with depth as pore spaces close due to vertical compaction (Athy 1930; Bahr *et al.* 2001). Resistor R3 stands out as a porosity anomaly.

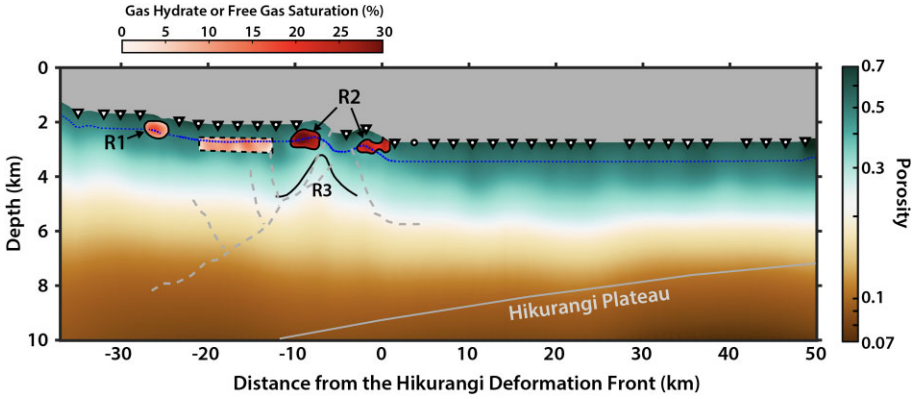

Figure 7. Resistivity-derived porosity and gas hydrate saturation for the Southern HT-RESIST profile calculated using the average resistivity of the preferred model from the joint CSEM-MT inversion (Fig. 6). The approximate base of the gas hydrate stability zone is shown as a blue dashed line. Key resistivity features are outlined in black. The grey solid and dashed lines are the approximate depth to the top of the Hikurangi Plateau and the estimated locations of thrust faults, respectively, from the SAHKE-01 seismic reflection data and velocity models in Mochizuki *et al.* (2019).

Given that it is situated below the base of the gas hydrate stability zone (BGHSZ), R3 is most likely associated with compressional tectonics in the forearc and the availability of dewatering pathways along thrust faults.

4.2 Consolidation state of the southern Hikurangi Margin inputs and protothrust zone development

Although the 2-D representation of porosity allows us to see how features in resistivity space map to porosity, it is difficult to identify other important features of the porosity and pore pressure that may exist in the model because the dominant porosity trend, particularly in the incoming sediment package, is due to vertical compaction (Athy 1930; Bahr *et al.* 2001; Morgan & Karig 1995). For that reason, it is useful to visualize relative, rather than absolute, porosity variations, which inform us about the consolidation state of the subduction inputs and of the accretionary wedge material. Ideally, a reference porosity model would be derived from sediment cores along this profile, but no such data are currently available.

Porosity-depth data from sediments of various localities have been shown to obey an exponential decay relationship, referred to as Athy's Law (Athy 1930; Bahr *et al.* 2001). Bahr *et al.* (2001) present an analytical justification of this exponential trend based on its physical underpinnings, namely compaction from sediment overburden. They demonstrate the agreement of this exponential trend with real data by fitting porosity data from marine sediment cores to exponential decay curves (Bahr *et al.* 2001). While an exponential curve cannot, of course, encapsulate all details of a given porosity-depth data set, it will approximate the overall compaction trend due to uniaxial stress. Thus it is reasonable to choose a reference porosity model that takes the form of a depth-parametrized decaying exponential.

Similar to the approach of Han *et al.* (2017), we define a reference compaction porosity model using a region of the 2-D resistivity-derived porosity model that is far enough seaward of the deformation front so as to be isolated from the effects of tectonic deformation. Barnes *et al.* (2018) note that the maximum width of the protothrust zone in the south-central Hikurangi Margin is 25 km, so we have chosen to average the porosities between 37 and 47 km seaward of the deformation front as the reference state of porosity for the Southern HT-RESIST profile. Using a single compaction model for the entire depth range leads to large misfits from the resistivity-derived porosity model for depths greater than ~2.5 kmbsf (Fig. S15). To avoid artificial trends that might arise because of the distinct lithologies and tectonic histories of sedimentary units in this region, we generated a separate compaction curve for each sharp velocity boundary identified in the *P*-wave model of Mochizuki *et al.* (2019), which are related to the lithological units from Bland *et al.* (2015). This approach is preferred to assuming a single exponential decay curve because it allows each lithology to be described by a unique set of prefactors and decay constants. To create the compaction curves, we fit a decaying exponential to each unit of every 1-D vertical profile through the porosity model from 37 to 47 km. We then averaged the compaction coefficients from these models to obtain a prefactor and decay constant of the exponential trend for each unit (Fig. 8). These values are given in Table 1. We obtain a porosity anomaly model by removing the reference compaction porosity model from the resistivity-derived porosity model.

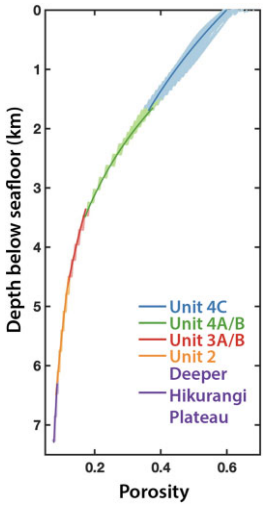

Figure 8. Compaction curves for the lithological units of the Southern HT-RESIST profile's incoming plate based on the average resistivity-derived porosities. Units are from Mochizuki *et al.* (2019). The shading is the porosity of each unit between between 37 and 47 km seaward of the deformation front. Solid lines are the compaction curves obtained by averaging the pre-exponential and decay constant terms from fitting the data from each porosity profile to an exponential decay equation. Parameters for these compaction curves are given in Table 1.

Table 1. Compaction curve parameters for porosity. These parameters were found by fitting the porosity averages from the 2-D model to the exponential model $\phi = \phi_0 e^{-cz}$, where ϕ is porosity, and z is depth below the top of the unit boundary in meters. See text for more details.

Unit ID	ϕ_0	c
4C	0.5991	2.957×10^{-4}
4A/B	0.7634	4.294×10^{-4}
3A/B	0.4628	2.932×10^{-4}
2	0.2865	1.910×10^{-4}
Deeper Hikurangi Plateau	0.1901	1.249×10^{-4}

A negative porosity anomaly is equivalent to overconsolidation and hence suggests relatively high effective stress and low pore pressures compared to a positive porosity anomaly. Because the compaction models only take into account vertical stress imparted by the overburden, we would expect the accretionary wedge material to have a negative porosity anomaly due to the additional horizontal strain from convergence unless this material cannot be drained efficiently. Indeed, the porosity anomaly is negative for most of the shallowest unit, Unit 4, in the accretionary wedge, but becomes positive with depth implying underconsolidation of and elevated fluid overpressures in the wedge and/or décollement. Because increased pore pressure decreases normal stress at the plate interface such conditions are thought to favor weak plate coupling (Audet & Schaeffer 2018), which does not match the observations of strong interplate coupling at the southern Hikurangi Margin (Wallace 2020). Though underconsolidation and heightened pore pressures are inferred in regions with reduced geodetic locking (e.g. Eberhart-Phillips *et al.* 2005, 2017; Han *et al.* 2017; Nakai *et al.* 2021), studies from the Alaska subduction zone have reported substantially higher pore pressures in the locked Semidi segment of the megathrust compared to the neighboring Shumagin Gap, which is poorly coupled (Li *et al.* 2018). Velocity data from the southern Hikurangi Margin have shown evidence for a weakly overpressured megathrust (Bassett *et al.* 2014), and this may also be indicated by its low taper angle (Saffer & Bekins 2002, 2006). Along with our porosity anomaly result, these observations imply that there is some threshold in the amount of overpressure required to favor creeping over locked conditions or that there is some temporal component to fluid pressure cycling that is not captured in these studies (Warren-Smith *et al.* 2019).

Permeability must also be considered when discussing wedge overpressure as low permeability inhibits drainage in the prism (Saffer & Bekins 2002, 2006). Our porosity anomaly results may indicate that permeability is high in the shallow accretionary wedge, but that the presence of a less permeable lithology inhibits the escape of fluids at depth. Thus, only the material in the shallow wedge becomes dewatered and feeds fluid seeps in the region (Watson *et al.* 2020). A thin section of high amplitude, subparallel reflections consisting of alternating layers of mudstones and nanofossil chalks (Sequence Y of Wood & Davy 1994) is found throughout the Pegasus Basin and has been identified as a potential seal for migrating fluids (Davy *et al.* 2008; Plaza-Faverola *et al.* 2012). This sequence has been mapped in the forearc above the décollement (Gase *et al.* 2022), where it may continue to impede dewatering and therefore contribute to excess overpressures at depth.

The porosity anomaly model also brings to light a key trend in the shallow Unit 4C sediments of the incoming plate (Fig. 9). This upper sediment package exhibits a notable reduction in porosity as it approaches the trench. Because this trend appeared upon removing the effects of compaction-related porosity reduction, it may be the result of lateral compressive stress, and implies that the hydrological response of the shallow incoming plate sediments to plate convergence occurs at least 20 km seaward of the trench in this region. We propose that this negative porosity anomaly is indicative of the development of a protothrust zone where additional sediment consolidation by tectonic compression has begun to reduce the porosity of the sediment package ahead of the frontal thrust. Reflection tomography of the nearby PEG09-23 seismic profile shows a trend in the velocity of the upper 1.5–2 km of incoming plate sediments that is consistent with the porosity anomaly seen here wherein V_p begins to increase around 18 km seaward of the deformation front. Interestingly, protothrusts are not readily apparent in the SAHKE-01 seismic reflection data (Bland *et al.* 2015; Mochizuki *et al.* 2019). If the porosity anomaly revealed by our EM data is indeed an accurate representation of the consolidation state of the sediments in this area, then it provides us with a snapshot of the hydrological conditions leading up to the formation of protothrusts, which will eventually translate the deformation front seaward.

Below the shallow sedimentary package, the porosity anomaly model displays the opposite trend—porosity increases relative to the reference model as the underlying sedimentary Units 4A/B and 3A/B approach the deformation front. The cause of this trend is not obvious, but may imply that the deeper sedimentary package experiences extensional, rather than compressive, stress near the trench. Because compression is no longer the dominant strain axis below the décollement (Morgan & Karig 1995), the change in the sign of the porosity anomaly from Unit 4C to Unit 4A/B might indicate that a younger décollement will form at this boundary. Cochrane *et al.* (1994) identified a velocity reversal below the sand unit of the protothrust zone offshore Cascadia, which they attributed either to a change in lithology or consolidation state. They classified the base of the sand unit as the protodécollement and suggest that a reduction in porosity at the boundary between the sands and underlying mudstones may lead to fluid entrapment and overpressure beneath the protodécollement. Wang *et al.* (1994) show that protothrust formation seaward of the frontal thrust requires heightened pore pressures in the incipient décollement. It is possible that the positive porosity anomaly of the deeper sediments is similarly suggestive of overpressured conditions, as were observed in the accretionary wedge. Currently, the décollement exists between Units 4A/B and 3A/B (Bland *et al.* 2015), so if the protodécollement is to form at the porosity anomaly reversal, it will require a step-up in the décollement.

Alternatively, the positive porosity anomaly of Units 4A/B and 3A/B could indicate the opening of tensional cracks and normal faults as the plate experiences intense bending in this region (Herath *et al.* 2020). Though subtle, the observed positive anomaly begins around the seaward-most normal fault interpreted in the SAHKE-01 seismic reflection profile (Henrys *et al.* 2013; Bland *et al.* 2015; Mochizuki *et al.* 2019), lending support to the argument that tensional stresses may be responsible for the anomaly. The ability of this sedimentary unit to fracture would imply that it is heavily indurated, perhaps even partially lithified, before it subducts.

Statistical analyses of subduction zone parameters and compilations of sediment thickness at subduction zones show that great earthquakes ($M_w \geq 8.5$) are more likely to nucleate on the longest subduction segments where a thick sediment package is being subducted (Wang & Bilek 2014; Scholl *et al.* 2015; Brizzi *et al.* 2018). The inversion in the sign of the porosity anomaly suggests that the upper sedimentary unit is decoupled from the deeper sediment package. Most of this thick, deeper sedimentary section should

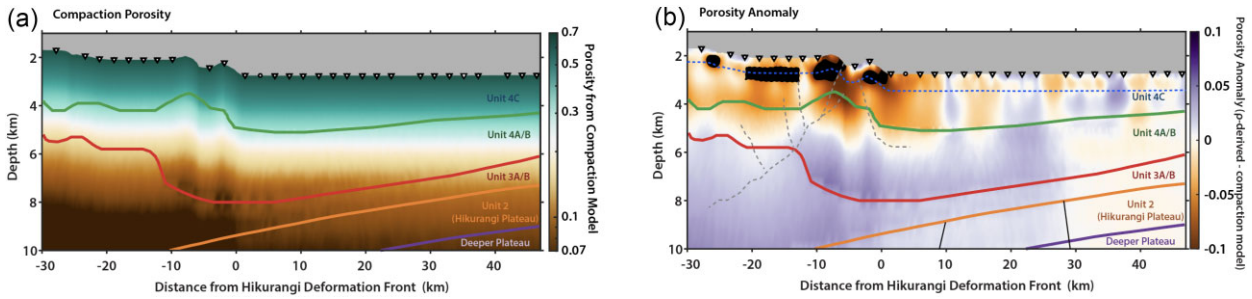

Figure 9. Reference compaction porosity model and porosity anomaly for the Southern HT-RESIST profile. Panel (a) shows the compaction porosity model derived from the curves in Fig. 8. (b) is the porosity anomaly calculated by removing the compaction porosity models from the resistivity-derived porosity (see Fig. 7). A negative porosity anomaly suggests that the porosity in Fig. 7 is less than what would be predicted from vertical compaction whereas a positive anomaly suggests a higher relative porosity than would be expected from compaction alone. Solid green, red, orange, and purple lines are the lithological unit boundaries from Mochizuki *et al.* (2019). Solid black lines and dashed grey lines in (b) are the approximate locations of normal faults in the Hikurangi Plateau and thrust faults in the accretionary wedge, respectively (Bland *et al.* 2015; Mochizuki *et al.* 2019). Dashed blue line is the estimated BSR depth. Proposed regions containing gas or hydrates are indicated by black shading.

therefore subduct with the Hikurangi Plateau. In studies of the minimally accreting south-central Chile subduction zone, it has been suggested that the smoothness of the plate interface, which can be attributed to the subduction of a thick (∼1.5 km) and well-drained sediment package, has allowed for higher levels of stress accumulation over broader areas than would be the case for regions with rough subduction (Olsen *et al.* 2020). Such a capacity for large stress accumulation may in turn contribute to why the Chile subduction zone has experienced some of the largest megathrust earthquakes in historical times (Olsen *et al.* 2020). The deeper sedimentary unit here may similarly act to smooth the interface in the southern Hikurangi Margin so that the upper plate is shielded from the roughness of the Hikurangi Plateau below (Gase *et al.* 2022). Analogue models of rough and smooth subducting slabs reveal that rougher slabs exhibit less interseismic coupling than smoother slabs and that smoother models produced larger rupture areas (van Rijsingen *et al.* 2019). Thus the subduction of this thick sediment package may help explain why interseismic coupling is much stronger in the southern Hikurangi Margin than to the north, where rough subduction is well-documented (Bell *et al.* 2010; Barker *et al.* 2018; Shaddox & Schwartz 2019; Barnes *et al.* 2020; Gase *et al.* 2021; Chesley *et al.* 2021; Gase *et al.* 2022).

The thickness of the sedimentary units in the southern Hikurangi Margin impedes a higher resolution at plate interface depths that was obtained in Chesley *et al.* (2021) and, therefore, precludes a detailed comparison between the northern and southern Hikurangi resistivity models. Nevertheless, the two models do show that the northern Hikurangi Margin has a much higher degree of heterogeneity in its resistivity structure than does the southern part of the margin, which translates to a greater complexity in the porosity of the incoming plate material in the north. It is unclear whether the inhomogeneity of the porosity structure, heterogeneity in lithology of the subducting protolith, considerable seafloor roughness, or some other factor drives the occurrence of shallow slow slip events in the northern Hikurangi Margin compared to their absence in the shallow megathrust of the south.

4.3 Gas hydrate in the accretionary wedge

Gas hydrates, compounds that contain gas, usually methane, bound in a solid lattice of water, are often a target of CSEM studies because their high resistivity relative to the seawater they displace in sediments makes them easily detectable by the active currents associated with an inline electric field (Weitemeyer *et al.* 2006; Constable 2010; Schwalenberg *et al.* 2010, 2017; Weitemeyer *et al.* 2011; Myer *et al.* 2012, 2015; Attias *et al.* 2018; Kannberg & Constable 2020). The potential use of gas hydrates in the energy industry has led to interest in quantifying their abundance in locations with extraction potential. Formation of these hydrates requires a relatively narrow high pressure, low temperature window, and such conditions are often met in the shallowest sediment layers of an accretionary wedge (Mienert 2022). The source for this gas may be thermogenic or biogenic in origin, and migration of the gas from its generation site into the gas hydrate stability zone can occur via advective or diffusive mechanisms. To estimate the approximate BGHSZ along our profile (see Figs 6 and 7), we calculated the depths at which the temperatures from the methane hydrate phase diagram given in Bohrmann & Torres (2014) would equal the temperature in the shallow sediments (see eq. 8).

Gas hydrate deposits have been recognized extensively at the Hikurangi Margin (Pecher *et al.* 2010; Crutchley *et al.* 2011, 2015; Mountjoy *et al.* 2014; Plaza-Faverola *et al.* 2012; Fraser *et al.* 2016; Koch *et al.* 2016; Schwalenberg *et al.* 2017; Han *et al.* 2021; Kroeger *et al.* 2022). Given the anomalously high resistivity of R1 and R2 (1.8–3.5 Ω-m) and their location above the BGHSZ, they likely indicate the presence of gas hydrate, although their resistivity could also be consistent with free gas. Typically, the strongest BSRs in the southern Hikurangi margin locate beneath ridges that have undergone compressional deformation and deeply penetrating thrust faults have been shown to act as conduits for focused fluid flow towards and through the gas hydrate system in this area (Pecher *et al.* 2010; Crutchley *et al.* 2011; Plaza-Faverola *et al.* 2012; Kroeger *et al.* 2022). Reduced permeability of anticlines often causes such folds to trap vertically migrating gas (Koch *et al.* 2016), and our resistivity model supports that observation for R2. It is also likely that R1 is located in a palaeo-anticline (Bland *et al.* 2015; Mochizuki *et al.* 2019).

Observations of thick free gas pockets beneath thrust ridges suggest that the thrust systems of the accretionary wedge play a key role in wedge dewatering (Crutchley *et al.* 2015). Additionally, high reflectivity segments that extend a limited distance from some BSRs indicate permeability-facilitated, layer-constrained hydrate precipitation from the migration of free gas into the gas hydrate stability zone (Crutchley *et al.* 2015). Thus, free gas can be brought to the

gas hydrate stability zone along thrust faults and is then able to accumulate and spread laterally via permeable strata above the BGHSZ (Crutchley *et al.* 2015; Wang *et al.* 2017; Kroeger *et al.* 2022). In general, this layer-restricted flow of gas would be consistent with a greater bulk layer normal resistance compared to the layer parallel resistance, and this agrees with our model, which shows higher vertical resistivity relative to horizontal resistivity in R1 and R2 (Fig. 6). It is possible that thrust faults beneath R2 have focused the flow of gas into the ridges and the boundaries between sedimentary units or the strata themselves have acted as permeable pathways along which gas can migrate (Plaza-Faverola *et al.* 2012; Crutchley *et al.* 2015; Fraser *et al.* 2016; Kroeger *et al.* 2022).

Interestingly, R1 and R2 lie mostly above the estimated BGHSZ, whereas the BGHSZ cuts through the middle of the less resistive connection between R1 and R2. This seems to further implicate R1 and R2 as concentrated gas hydrate accumulations. Concentrated gas hydrate deposits imply that a mechanism exists for direct fluid flow from depth (Wang *et al.* 2017), and such a migration of methane through the accretionary wedge should influence fluid pressure in the forearc. The less resistive connection between R1 and R2 may also be associated with gas fed from the major and antithetical thrust faults of the accretionary wedge, although diffuse flow of the gas that ponds at the BGHSZ may alternatively be responsible for supplying gas to this resistor. Whatever mechanisms contribute to transporting gas to this location seem unable to transfer the gas even shallower, preventing some formation of solid clathrate.

Gas hydrate saturation can be estimated from resistivity using Archie's Law (Archie 1942) in the following form:

$$S_{\text{gas}} = 1 - \left(\frac{\rho_f}{\phi^m \rho} \right)^{\frac{1}{n}}, \tag{12}$$

where S_{gas} is the saturation of gas hydrate, and as before (see eq. 6), ρ_f is the resistivity of the seawater, ρ is the measured bulk resistivity, ϕ is the porosity of the unit and m is the cementation exponent. We let the saturation exponent $n = 2$ after Schwalenberg *et al.* (2017). Because no cores or well logs exist along this profile we use our porosity model to estimate ϕ in eq. (12). As in Section 4.1, we seek a 1-D compaction model for the shallow forearc. We isolate the region from −30 to −24 km and from 0.2 kmbsf to 1.5 kmbsf. We then remove any parts of the model where the vertical resistivity is $\geq$1.8 Ω-m, values which suggest gas hydrate or free gas is present. We then fit a decaying exponential to each 1-D profile extracted from what remains of the porosity model and average all of the estimated compaction curve parameters to define a single compaction model (Fig. S16). This is the compaction-based porosity model we use to approximate ϕ in eq. (12).

Fig. 7 shows the calculated gas hydrate saturation for R1, R2 and the diffuse resistive connection between these more prominent resistors. Our data suggest that gas hydrate (or free gas) saturation as high as 17 and 33 per cent may be expected in R1 and R2, respectively. Of course, compaction is not the only control on porosity in an accretionary wedge, where lateral shortening also leads to expulsion of pore fluids and extension at the apex of anticlines may increase porosity. Therefore, the compaction curve, which we have generated using porosities from the landward side of the forearc, does not take into account spatial variability in the additional tectonic forces that affect accretionary wedge porosity. The saturation estimates will thus be more accurate for R1 and the diffuse connection between R1 and R2 than they will be for R2, which may be undergoing additional deformation. Even so, our data indicate where pockets of the Southern Hikurangi forearc are highly saturated with free gas or gas hydrate.

4.4 Resistivity properties of margin thrust faults

At present, depth-migrated seismic data are not available for SAHKE-01, the seismic reflection profile that is co-located with our southern Hikurangi resistivity data. However, from the interpreted TWTT section of Bland *et al.* (2015) and velocity model of Mochizuki *et al.* (2019), it appears that the landward edge of resistor R3 is bounded by a major thrust fault in the forearc such that R3 forms the footwall of this fault. The heightened resistivity of R3 implies either that the footwall has undergone significant compression compared to the hanging wall, the footwall contains large quantities of trapped gas, or that the hanging wall is heavily fractured. If the former interpretation is appropriate, then it suggests that porosity reduction by heterogeneous horizontal compaction has led to an average porosity of the footwall (0.27) that is 16 per cent less than that of the hanging wall (0.32). For rapid thrusting or low permeability sediments, this observation of a more resistive footwall with respect to the hanging wall contrasts what has been observed in the field (Cochrane *et al.* 1994; Screaton *et al.* 2002; Bangs *et al.* 2004; Hamahashi *et al.* 2013; Flemings & Saffer 2018) and in numerical simulations (Sun *et al.* 2020b, a). Typically, it may be expected that the footwall should be more conductive than the hanging wall because the material that comprises the hanging wall was buried more deeply, and should thus have been more consolidated, than that of the footwall prior to thrust displacement. A more resistive footwall might imply that high permeability in the footwall allowed for faster drainage and subsequent lateral compression to close pore spaces more efficiently in the footwall. This could be the result of lithological differences between the footwall and the hanging wall wherein the footwall contains material that drains more readily than that of the hanging wall. Alternatively, asymmetric damage may have led to more intense fracturing in the hanging wall relative to the footwall, as is the case for the Pāpaku Fault along the Northern HT-RESIST profile (Savage *et al.* 2021). Such fractures would potentially form well-connected fluid pathways. And, as mentioned before, we cannot rule out the possibility that the pore spaces of R3 contain some non-trivial amount of gas, making this feature more akin to a gas chimney. Other types of geophysical and geochemical data could help narrow down these possibilities.

5 CONCLUSIONS

In this study, we have modelled the resistivity along the southern Hikurangi Margin using marine CSEM and MT data. Shallow resistors in the forearc indicate the presence of free gas or gas hydrate in the accretionary wedge with saturation as high as 33 per cent. A deeper resistor beneath the forearc ridges locates in the footwall of a major thrust fault, which may imply the presence of small amounts of gas or more rapid pore closure in the footwall compared to the hanging wall.

Converting our resistivity model into porosity confirms that vertical compaction is the dominant control on porosity. Removal of a background compaction trend gives us insight into the consolidation state of the incoming plate sediments and the accretionary wedge. Negative porosity anomalies in the shallow units of the accretionary wedge indicate overconsolidation and efficient drainage, whereas positive porosity anomalies in the deeper forearc suggest

overpressured conditions and the inability of some fluids to escape the system. Although heightened fluid pore pressures generally seem to favor aseismic creep, geodetic data show that the southern Hikurangi Margin exhibits strong plate coupling. Thus our observation of underconsolidation deeper in the wedge could imply that a threshhold pore pressure is necessary to promote aseismic creep where thick sediment packages are being subducted.

The porosity anomaly for the incoming plate illuminates a trend wherein the shallow sediments become increasingly overconsolidated upon approaching the trench. This observation is consistent with the early stages in the formation of a protothrust zone at least 20 km seaward of the main frontal thrust. Positive porosity anomalies in the deeper sediment units of the incoming plate may imply a change from mainly compressive to extensional stresses. This reversal could cause a step-up in the décollement with time, which would lead to the subduction of an even thicker sediment package that acts to smooth the plate interface and promote strong interseismic coupling.

SUPPORTING INFORMATION

Supplementary data are available at *GJI* online.

Figure S1. Deployment duration and depth for each ocean-bottom electromagnetometer. The upper panel purple bar graph shows the length of time each receiver was recording on the seafloor for this survey. The bottom panel orange bar graph shows the depth at which each receiver settled on the seafloor.

Figure S2. Anisotropy ratios (ρ_v/ρ_h) for: (a) CSEM-only (Figs 5a and b), (b) MT-only (Figs 5c and d) and (c) joint inversions (Fig. 6). The largest anisotropy ratios are apparent in the joint inversion because of the preferential sensitivities of the CSEM and MT data to vertical and horizontal resistivity, respectively.

Figure S3. Sensitivity analysis for resistors R1 and R2 in the forearc. CSEM data from the odd-numbered receivers in the forearc (s23, s27, s29, s31 and s35) were excluded and a joint inversion of the remaining CSEM data and all MT data was run from a 1 Ω-m half-space starting model. The RMS misfit of the final model shown here is 1.002. Receivers with MT data are depicted as inverted, black triangles and those with CSEM data as pink circles. Vertical (horizontal) resistivity with and without the interpretations from Fig. 6 are shown in (a) and (b), (c) and (d), respectively. The resistors are still present in the model even with the exclusion of the odd receivers. No additional resistors have been added in the new data gaps.

Figure S4. Sensitivity analysis for resistors R1 and R2 in the forearc. CSEM data from the even-numbered receivers in the forearc (s24, s26, s30, s32 and s34) were excluded and a joint inversion of the remaining CSEM data and all MT data was run from a 1 Ω-m half-space starting model. The RMS misfit of the final model shown here is 1.010. Receivers with MT data are depicted as inverted, black triangles and those with CSEM data as pink circles. Vertical (horizontal) resistivity with and without the interpretations from Fig. 6 are shown in (a) and (b), (c) and (d), respectively. The resistors are still present in the model even with the exclusion of the even receivers. No additional resistors have been added in the new data gaps.

Figure S5. Normalized RMS misfits for CSEM (top panel) and MT (bottom panel) data based on the preferred model (Fig. 6). Dashed black line shows where RMS = 1. The blue and red circles are normalized residuals for all inline electric field amplitude and phase data, respectively, at a given transmitter position. The bars are RMS misfit for impedance tensor components of each MT receiver: blue, TE mode apparent resistivity; green, TE phase; orange, TM mode apparent resistivity; purple, TM phase.

Figure S6. CSEM data (top panel), model fits (middle panel) and normalized residuals (bottom panel) as a function of distance from the Hikurangi Margin and transmitter-receiver offset for the 0.25 Hz (fundamental) frequency. Left-hand column is amplitude and right-hand column is phase.

Figure S7. CSEM data (top panel), model fits (middle panel) and normalized residuals (bottom panel) as a function of distance from the Hikurangi Margin and transmitter–receiver offset for the 0.75 Hz frequency. Left-hand column is amplitude and right-hand column is phase.

Figure S8. CSEM data (top panel), model fits (middle panel) and normalized residuals (bottom panel) as a function of distance from the Hikurangi Margin and transmitter–receiver offset for the 1.75 Hz frequency. Left-hand column is amplitude and right-hand column is phase.

Figure S9. Fit of the preferred resistivity model (lines) to MT data (circles) from receivers s01 to s10. TE mode is blue and TM mode is red.

Figure S10. Fit of the preferred resistivity model (lines) to MT data (circles) from receivers s12 to s20. TE mode is blue and TM mode is red.

Figure S11. Fit of the preferred resistivity model (lines) to MT data (circles) from receivers s22 to s31. TE mode is blue and TM mode is red.

Figure S12. Fit of the preferred resistivity model (lines) to MT data (circles) from receivers s32 to s37. TE mode is blue and TM mode is red.

Figure S13. Sensitivity analysis for the presence of a resistive connection between R1 and R2 in which a fixed resistivity of 1.5 and 1 Ω-m in the vertical and horizontal directions, respectively, was assigned to the outlined rectangle before inverting the remaining model space. (a) and (b) are the inversion results for resistivity in the vertical and horizontal directions, respectively. (c) and (d) show the differences between resistivity in this inversion and that of the preferred model (Fig. 6) in the area near the fixed resistivity patch (black rectangle). This model fits the data well (RMS = 1.000), but note that resistivity has increased directly above and below the patch of fixed resistivity in this model compared to that of the preferred model. This implies that a resistive connection between R1 and R2 is required.

Figure S14. Variations in the modified Archie's denominator of Sen & Goode (1992) as a function of pore fluid conductivity. Each panel shows a different pore fluid temperature from 0 to 105 °C. Green and brown lines show changes in R and $R + \sigma_f$, which is the modified Archie denominator from eq. (9), as a function of the pore fluid resistivity. Dashed blue line highlights where conductivity equals that of the pore fluid. Dotted, vertical black line indicates seawater conductivity at each of these temperatures. Note that the modified denominator is approximately equal to the pore fluid conductivity for pore fluids that are at least as conductive as seawater. This is especially true at lower temperatures. Thus Archie's law is roughly equivalent to the modified law when seawater is the pore fluid.

Figure S15. Comparison between a single compaction model (solid black line) from 37 to 47 km along the profile to the compaction models in Fig. 8 that were generated for each lithological unit in Mochizuki *et al.* (2019). Solid lines are the compaction models and points forming a shaded region are the porosities from Fig. 7. The single compaction curve deviates from the porosity data at all depths, but particularly at depths greater than ∼2.5 kmbsf.

Figure S16. Compaction curves for the shallow forearc of the southern HT-RESIST profile for the (a) vertical and (b) horizontal porosities. The magenta dots are porosity taken from −30 to −24 km in Fig. 7. The solid black lines are the compaction curves derived from averaging the pre-exponential and decay constant terms from fitting the data from each vertical porosity profile to an exponential decay equation.

Please note: Oxford University Press is not responsible for the content or functionality of any supporting materials supplied by the authors. Any queries (other than missing material) should be directed to the corresponding author for the paper.

ACKNOWLEDGMENTS

We thank Scripps Institution of Oceanography for providing the instrumentation necessary to collect the EM data used in this study, the New Zealand government for permission to work in their exclusive economic zone and the captains (W. Hill and D. Murline) and crew of the R/V Revelle Expeditions RR1817 and RR1903. Many thanks to S. Constable and the Scripps Marine EM Lab (C. Armerding, J. Lemire, J. Perez, J. Souders) and the HT-RESIST science party (A. Adams, J. Alvarez-Aramberri, C. Armerding, E. Attias, E.A. Bertrand, D. Blatter, G. Boren, G. Franz, C. Gustafson, W. Heise, Y. Li, B. Oryan, N. Palmer, J. Perez, J. Sherman, K. Woods and A. Yates). We thank the National Institute of Water and Atmospheric Research (NIWA; https://niwa.co.nz/) for providing high-resolution bathymetry data. This work was supported by the National Science Foundation grant OCE-1737328. CC acknowledges funding support by the Department of Defense (DoD) through the National Defense Science and Engineering Graduate (NDSEG) Fellowship Program. We acknowledge computing resources from Columbia University's Shared Research Computing Facility project, which is supported by NIH Research Facility Improvement Grant 1G20RR030893-01. We also thank Anne Bécel and Demian Saffer for the insightful discussions.

DATA AVAILABILITY

All EM data that were inverted and analysed in this study are available at https://doi.org/10.5281/zenodo.7972304. The MARE2DEM code used to invert the data along with a description of the data file format are available at: http://mare2dem.bitbucket.io.

REFERENCES

Archie, G., 1942. The electrical resistivity log as an aid in determining some reservoir characteristics, *Trans. AIME,* **146**(1), 54–62.

Athy, L. F., 1930. Density, porosity, and compaction of sedimentary rocks, *AAPG Bull.,* **14**(1), 1–24.

Attias, E. *et al.*, 2018. High-resolution resistivity imaging of marine gas hydrate structures by combined inversion of CSEM towed and ocean-bottom receiver data, *Geophys. J. Int.,* **214**(3), 1701–1714.

Attias, E., Thomas, D., Sherman, D., Ismail, K. & Constable, S., 2020. Marine electrical imaging reveals novel freshwater transport mechanism in Hawai'i, *Sci. Adv.,* **6**(48), 1–9, doi:10.1126/sciadv.abd4866.

Audet, P. & Schaeffer, A.J., 2018. Fluid pressure and shear zone development over the locked to slow slip region in Cascadia, *Sci. Adv.,* **4**(3), 1–7.

Bahr, D.B., Hutton, E.W., Syvitski, J.P. & Pratson, L.F., 2001. Exponential approximations to compacted sediment porosity profiles, *Comput. Geosci.,* **27**(6), 691–700.

Bangs, N.L., Shipley, T.H., Gulick, S.P., Moore, G.F., Kuromoto, S. & Nakamura, Y., 2004. Evolution of the nankai Trough décollement from the trench into the seismogenic zone: inferences from three-dimensional seismic reflection imaging, *Geology,* **32**(4), 273–276.

Barker, D. H.N., Sutherland, R., Henrys, S. & Bannister, S., 2009. Geometry of the Hikurangi subduction thrust and upper plate, North Island, New Zealand, *Geochem. Geophys. Geosyst.,* **10**(2), doi:10.1029/2008GC002153.

Barker, D. H.N., Henrys, S., Tontini, F.C., Bassett, D., Todd, E. & Wallace, L., 2018. Geophysical constraints on the relationship between seamount subduction, slow slip, and tremor at the North Hikurangi subduction zone, New Zealand, *Geophys. Res. Lett.,* **45,** 804–813.

Barnes, P.M. *et al.*, 2010. Tectonic and geological framework for gas hydrates and cold seeps on the Hikurangi subduction margin, New Zealand, *Mar. Geol.,* **272**(1–4), 26–48.

Barnes, P.M., Ghisetti, F.C., Ellis, S. & Morgan, J.K., 2018. The role of protothrusts in frontal accretion and accommodation of plate convergence, Hikurangi subduction margin, New Zealand, *Geosphere,* **14**(2), 440–468.

Barnes, P.M. *et al.*, 2020. Slow slip source characterized by lithological and geometric heterogeneity, *Sci. Adv.,* **6,** 1–11.

Bassett, D., Sutherland, R. & Henrys, S., 2014. Slow wavespeeds and fluid overpressure in a region of shallow geodetic locking and slow slip, Hikurangi subduction margin, New Zealand, *Earth planet. Sci. Lett.,* **389,** 1–13.

Bekins, B.A. & Dreiss, S.J., 1992. A simplified analysis of parameters controlling dewatering in accretionary prisms, *Earth planet. Sci. Lett.,* **109**(3-4), 275–287.

Bell, R., Sutherland, R., Barker, D.H., Henrys, S., Bannister, S., Wallace, L. & Beavan, J., 2010. Seismic reflection character of the Hikurangi subduction interface, New Zealand, in the region of repeated Gisborne slow slip events, *Geophys. J. Int.,* **180**(1), 34–48.

Bland, K.J., Uruski, C.I. & Isaac, M.J., 2015. Pegasus Basin, eastern New Zealand: a stratigraphic record of subsidence and subduction, ancient and modern, *N. Zeal. J. Geol. Geophys.,* **58**(4), 319–343.

Bohrmann, G. & Torres, M.E., 2014. Marine gas hydrates, *Encyclopedia of Marine Geosciences,* pp. 1–7, Springer.

Bray, C.J. & Karig, D.E., 1985. Porosity of sediments in accretionary prisms and some implications for dewatering processes., *J. geophys. Res.,* **90**(B1), 768–778.

Brizzi, S., Sandri, L., Funiciello, F., Corbi, F., Piromallo, C. & Heuret, A., 2018. Multivariate statistical analysis to investigate the subduction zone parameters favoring the occurrence of giant megathrust earthquakes, *Tectonophysics,* **728–729,** 92–103.

Chave, A.D. & Weidelt, P., 2012. The theoretical basis for electromagnetic induction, in *The Magnetotelluric Method Theory and Practice,* Chapter 2, pp. 19–49, eds Chave, Alan D. & Jones, Alan G., Cambridge Univ. Press.

Chesley, C., Key, K., Constable, S., Behrens, J. & Macgregor, L., 2019. Crustal cracks and frozen flow in oceanic lithosphere inferred from electrical anisotropy, *Geochem. Geophys. Geosyst.,* **20,** 1–21.

Chesley, C., Naif, S., Key, K. & Bassett, D., 2021. Fluid-rich subducting topography generates anomalous forearc porosity, *Nature,* **595,** 255–260.

Clark, K.J., Hayward, B.W., Cochran, U.A., Wallace, L.M., Power, W.L. & Sabaa, A.T., 2015. Evidence for past subduction earthquakes at a plate boundary with widespread upper plate faulting: Southern Hikurangi Margin, New Zealand, *Bull. seism. Soc. Am.,* **105**(3), 1661–1690.

Cochrane, G.R., Moore, J.C., Mackay, M.E. & Moore, G.F., 1994. Velocity and inferred porosity model of the Oregon accretionary prism for multichannel seismic reflection data: Implications on sediment dewatering and overpressure, *J. geophys. Res.,* **99**(B4), 7033–7043.

Constable, S., 2010. Ten years of marine CSEM for hydrocarbon exploration, *Geophysics,* **75**(5), 75A67–75A81.

Constable, S., 2013. Review paper: instrumentation for marine magnetotelluric and controlled source electromagnetic sounding, *Geophys. Prospect.,* **61**(Suppl. 1), 505–532.

Constable, S., Key, K. & Lewis, L., 2009. Mapping offshore sedimentary structure using electromagnetic methods and terrain effects in marine magnetotelluric data, *Geophys. J. Int.,* **176,** 431–442.

Constable, S.C., Parker, R.L. & Constable, C.G., 1987. Occam's inversion: a practical algorithm for generating smooth models from electromagnetic sounding data., *Geophysics,* **52**(3), 289–300.

Crutchley, G.J., Gorman, A.R., Pecher, I.A., Toulmin, S. & Henrys, S.A., 2011. Geological controls on focused fluid flow through the gas hydrate stability zone on the southern Hikurangi Margin of New Zealand, evidenced from multi-channel seismic data, *Mar. Petrol. Geol.,* **28**(10), 1915–1931.

Crutchley, G.J., Fraser, D.R., Pecher, I.A., Gorman, A.R., Maslen, G. & Henrys, S.A., 2015. Gas migration into gas hydrate-bearing sediments on the southern Hikurangi margin of New Zealand, *J. geophys. Res.,* **120**(2), 725–743.

Crutchley, G.J., Kroeger, K.F., Pecher, I.A. & Gorman, A.R., 2018. How tectonic folding influences gas hydrate formation: New Zealand's Hikurangi subduction margin, *Geology,* **47**(1), 39–42.

Crutchley, G.J., Klaeschen, D., Henrys, S.A., Pecher, I.A., Mountjoy, J.J. & Woelz, S., 2020. Subducted sediments, upper-plate deformation and dewatering at New Zealand's southern Hikurangi subduction margin, *Earth planet. Sci. Lett.,* **530,** 1–14.

Davy, B., 2014. Rotation and offset of the Gondwana convergent margin in the New Zealand region following Cretaceous jamming of Hikurangi Plateau large igneous province subduction, *Tectonics,* **33,** 1577–1595.

Davy, B., Hoernle, K. & Werner, R., 2008. Hikurangi Plateau: crustal structure, rifted formation, and Gondwana subduction history, *Geochem. Geophys. Geosyst.,* **9**(7), doi:10.1029/2007GC001855.

Dominguez, S., Lallemand, S.E., Malavieille, J. & Von Huene, R., 1998. Upper plate deformation associated with seamount subduction, *Tectonophysics,* **293**(3–4), 207–224.

Dominguez, S., Malavieille, J. & Lallemand, S.E., 2000. Deformation of accretionary wedges in response to seamount subduction: Insights from sandbox experiments, *Tectonics,* **19**(1), 182–196.

Du, Z. & Key, K., 2018. Case study: North Sea heavy oil reservoir characterization from integrated analysis of towed-streamer em and dual-sensor seismic data, *Leading Edge,* **37**(8), 608–615.

Eberhart-Phillips, D., Reyners, M., Chadwick, M. & Chiu, J.M., 2005. Crustal heterogeneity and subduction processes: 3-D Vp, Vp/Vs and Q in the southern North Island, New Zealand, *Geophys. J. Int.,* **162**(1), 270–288.

Eberhart-Phillips, D., Bannister, S. & Reyners, M., 2017. Deciphering the 3-D distribution of fluid along the shallow Hikurangi subduction zone using P-and S-wave attenuation, *Geophys. J. Int.,* **211,** 1032–1045.

Egbert, G.D., 1997. Robust multiple-station magnetotelluric data processing, *Geophys. J. Int.,* **130**(2), 475–496.

Evans, R.L., 1994. Constraints on the large-scale porosity and permeability structure of young oceanic crust from velocity and resistivity data, *Geophys. J. Int.,* **119**(3), 869–879.

Flemings, P.B. & Saffer, D.M., 2018. Pressure and stress prediction in the Nankai accretionary prism: a critical state soil mechanics porosity-based approach, *J. geophys. Res.,* **123**(2), 1089–1115.

Fohrmann, M. & Pecher, I.A., 2012. Analysing sand-dominated channel systems for potential gas-hydrate-reservoirs using an AVO seismic inversion technique on the Southern Hikurangi Margin, New Zealand, *Mar. Petrol. Geol.,* **38**(1), 19–34.

Fraser, D.R., Gorman, A.R., Pecher, I.A., Crutchley, G.J. & Henrys, S.A., 2016. Gas hydrate accumulations related to focused fluid flow in the Pegasus Basin, southern Hikurangi Margin, New Zealand, *Mar. Petrol. Geol.,* **77,** 399–408.

Gase, A.C., Avendonk, H. J. A.V., Bangs, N.L., Bassett, D. & Stuart, A., 2021. Crustal structure of the northern Hikurangi margin, New Zealand : variable accretion and overthrusting plate strength influenced by rough subduction, *J. geophys. Res.,* **126**(5), doi:10.1029/2020JB021176.

Gase, A.C., Bangs, N.L., Avendonk, H. J. A.V., Bassett, D. & Henrys, S.A., 2022. Hikurangi megathrust slip behavior influenced by lateral variability in sediment subduction, *Geology,* **50**(10), 1145–1149.

Guo, C., Fan, Z., Ling, B. & Yang, Z., 2022. A tensorial Archie's law for water saturation evaluation in anisotropic model, *IEEE Geosci. Remote Sens. Lett.,* **19,** 1–5.

Gurnis, M. *et al.*, 2019. Incipient subduction at the contact with stretched continental crust: the Puysegur Trench, *Earth planet. Sci. Lett.,* **520,** 212–219.

Gustafson, C., Key, K. & Evans, R.L., 2019. Aquifer systems extending far offshore on the U.S. Atlantic margin, *Sci. Rep.,* **9**(1), 1–10.

Hamahashi, M. *et al.*, 2013. Contrasts in physical properties between the hanging wall and footwall of an exhumed seismogenic megasplay fault in a subduction zone - an example from the Nobeoka Thrust Drilling Project, *Geochem. Geophys. Geosyst.,* **14**(12), 5354–5370.

Han, S., Bangs, N.L., Carbotte, S.M., Saffer, D.M. & Gibson, J.C., 2017. Links between sediment consolidation and Cascadia megathrust slip behaviour, *Nat. Geosci.,* **10**(12), 954–959.

Han, S., Bangs, N.L., Hornbach, M.J., Pecher, I.A., Tobin, H.J. & Silver, E.A., 2021. The many double BSRs across the northern Hikurangi margin and their implications for subduction processes, *Earth planet. Sci. Lett.,* **558,** 116743.

Henrys, S. *et al.*, 2013. SAHKE geophysical transect reveals crustal and subduction zone structure at the southern Hikurangi margin, New Zealand, *Geochem. Geophys. Geosyst.,* **14**(7), 2063–2083.

Herath, P., Stern, T.A., Savage, M.K., Bassett, D., Henrys, S. & Boulton, C., 2020. Hydration of the crust and upper mantle of the Hikurangi Plateau as it subducts at the southern Hikurangi margin, *Earth planet. Sci. Lett.,* **541,** doi:10.1016/j.epsl.2020.116271.

Hoernle, K., Hauff, F., van den Bogaard, P., Werner, R., Mortimer, N., Geldmacher, J., Garbe-Schönberg, D. & Davy, B., 2010. Age and geochemistry of volcanic rocks from the Hikurangi and Manihiki oceanic Plateaus, *Geochim. Cosmochim. Acta,* **74**(24), 7196–7219.

Hyndman, R.D., Yuan, T. & Moran, K., 1999. The concentration of deep sea gas hydrates from downhole electrical resistivity logs and laboratory data, *Earth planet. Sci. Lett.,* **172**(1–2), 167–177.

International Ocean Discovery Program, 2021. *Expedition Statistics*. https://www.iodp.org/expeditions/expedition-statistics.

Ito, G. & Moore, G.F., 2021. Widths of imbricate thrust blocks and the strength of the front of accretionary wedges and fold-and-thrust belts, *Tectonophysics,* **799,** doi:10.1016/j.tecto.2020.228704.

Jiao, R., Seward, D., Little, T.A. & Kohn, B.P., 2014. Thermal history and exhumation of basement rocks from Mesozoic to Cenozoic subduction cycles, central North Island, New Zealand, *Tectonics,* **33**(10), 1920–1935.

Johansen, S.E., Panzner, M., Mittet, R., Amundsen, H. E.F., Lim, A., Vik, E. & Landrø, M., 2019. Deep electrical imaging of the ultraslow-spreading Mohns Ridge, *Nature,* **567,** 379–383.

Kannberg, P.K. & Constable, S., 2020. Characterization and quantification of gas hydrates in the California Borderlands, *Geophys. Res. Lett.,* **47**(6), 1–8.

Kennedy, W.D., Herrick, D.C. & Yao, T., 2001. Calculating water saturation in electrically anisotropic media, *Petrophysics,* **42**(2), 118–136.

Key, K., 2016. MARE2DEM: a 2-D inversion code for controlled-source electromagnetic and magnetotelluric data, *Geophys. J. Int.,* **207,** 571–588.

Key, K. & Constable, S., 2021. Inverted long-baseline acoustic navigation of deep-towed CSEM transmitters and receivers, *Mar. Geophys. Res.,* **42**(6), doi:10.1007/s11001-021-09427-z.

Koch, S. *et al.*, 2016. Gas migration through Opouawe Bank at the Hikurangi margin offshore New Zealand, *Geo-Mar. Lett.,* **36**(3), 187–196.

Kroeger, K.F., Crutchley, G.J., Hillman, J.I., Turco, F. & Barnes, P.M., 2022. Gas hydrate formation beneath thrust ridges: a test of concepts using 3D modelling at the southern Hikurangi Margin, New Zealand, *Mar. Petrol. Geol.,* **135,** 1–18, doi:10.1016/j.marpetgeo.2021.105394.

Li, J. *et al.*, 2018. Connections between subducted sediment, pore-fluid pressure, and earthquake behavior along the Alaska megathrust, *Geology,* **46**(4), 299–302.

Litchfield, N., Ellis, S., Berryman, K. & Nicol, A., 2007. Insights into subduction-related uplift along the Hikurangi Margin, New Zealand, using numerical modelling, *J. geophys. Res.,* **112**(F2), doi:10.1029/2006JF000535.

Liu, Y. & Kitanidis, P.K., 2013. Tortuosity and Archie's Law, in *Advances in Hydrogeology, Chapter 6,* pp. 115–126, Mishra, P. & Kuhlman, K., Springer.

Marone, C. & Scholz, C.H., 1988. The depth of seismic faulting and the upper transition from stable to unstable slip regimes, *Geophys. Res. Lett.,* **15**(6), 621–624.

Martí, A., 2014. The role of electrical anisotropy in magnetotelluric responses: from modelling and dimensionality analysis to inversion and interpretation, *Surv. Geophys.,* **35**(1), 179–218.

Micallef, A. *et al.*, 2020. 3D characterisation and quantification of an offshore freshened groundwater system in the Canterbury Bight, *Nat. Commun.,* **11**(1), doi:10.1038/s41467-020-14770-7.

Mienert, J., 2022. *World Atlas of Submarine Gas Hydrates in Continental Margins,* Springer Nature Switzerland.

Mochizuki, K. *et al.*, 2019. Recycling of depleted continental mantle by subduction and plumes at the Hikurangi Plateau large igneous province, southwestern Pacific Ocean, *Geology,* **47**(8), 1–4.

Moore, J.C. & Vrolijk, P., 1992. Fluids in accretionary prisms, *Rev. Geophys.,* **30**(2), 113–135.

Morgan, J.K. & Karig, D.E., 1995. Décollement processes at the Nankai accretionary margin, southeast Japan: propagation, deformation, and dewatering, *J. geophys. Res.,* **100**(B8), 15 221–15 231.

Mountjoy, J.J., Pecher, I., Henrys, S., Crutchley, G., Barnes, P.M. & Plaza-Faverola, A., 2014. Shallow methane hydrate system controls ongoing, downslope sediment transport in a low-velocity active submarine landslide complex, Hikurangi Margin, New Zealand, *Geochem. Geophys. Geosyst.,* **15**(11), 4137–4156.

Myer, D., Constable, S. & Key, K., 2011. Broad-band waveforms and robust processing for marine CSEM surveys, *Geophys. J. Int.,* **184**(2), 689–698.

Myer, D., Constable, S., Key, K., Glinsky, M.E. & Liu, G., 2012. Marine CSEM of the Scarborough gas field, Part 1: experimental design and data uncertainty, *Geophysics,* **77**(4), E281–E299.

Myer, D., Key, K. & Constable, S., 2015. Marine CSEM of the Scarborough gas field, Part 2: 2D inversion, *Geophysics,* **80**(3), E187–E196.

Naif, S., Key, K., Constable, S. & Evans, R.L., 2015. Water-rich bending faults at the Middle America Trench, *Geochem. Geophys. Geosyst.,* **16,** 2582–2597.

Naif, S., Key, K., Constable, S. & Evans, R.L., 2016. Porosity and fluid budget of a water-rich megathrust revealed with electromagnetic data at the Middle America Trench, *Geochem. Geophys. Geosyst.,* **17,** 2825–2834.

Naif, S., Selway, K., Murphy, B.S., Egbert, G. & Pommier, A., 2021. Electrical conductivity of the lithosphere-asthenosphere system, *Phys. Earth planet. Inter.,* **313,** doi:10.1016/j.pepi.2021.106661.

Nakai, J.S., Sheehan, A.F., Abercrombie, R.E. & Eberhart-Phillips, D., 2021. Near trench 3D seismic attenuation offshore Northern Hikurangi Subduction Margin, North Island, New Zealand, *J. geophys. Res.,* **126**(3), 1–20.

Newman, G.A., Commer, M. & Carazzone, J.J., 2010. Imaging CSEM data in the presence of electrical anisotropy, *Geophysics,* **75**(2), F51–F61.

Olsen, K.M., Bangs, N.L., Tréhu, A.M., Han, S., Arnulf, A. & Contreras-Reyes, E., 2020. Thick, strong sediment subduction along south-central Chile and its role in great earthquakes, *Earth planet. Sci. Lett.,* **538,** doi:10.1016/j.epsl.2020.116195.

Pecher, I.A. *et al.*, 2010. Focussed fluid flow on the Hikurangi Margin, New Zealand - evidence from possible local upwarping of the base of gas hydrate stability, *Mar. Geol.,* **272**(1–4), 99–113.

Pezard, P.A., Howard, J.J. & Lovell, M.A., 1989. Clay conduction and pore structure of oceanic basalts from DSDP/ODP Hole 504B, *Proc. the Ocean Drilling Prog., Sci. Results,* **111,** 97–108.

Plaza-Faverola, A., Klaeschen, D., Barnes, P., Pecher, I., Henrys, S. & Mountjoy, J., 2012. Evolution of fluid expulsion and concentrated hydrate zones across the southern Hikurangi subduction margin, New Zealand: an analysis from depth migrated seismic data, *Geochem. Geophys. Geosyst.,* **13**(8), doi:10.1029/2012GC004228.

Revil, A., Cathles, L.M., Losh, S. & Nunn, J.A., 1998. Electrical conductivity in shaly sands with geophysical applications, *J. geophys. Res.,* **103**(10), 23 925–23 936.

Reyners, M., 2013. The central role of the Hikurangi Plateau in the Cenozoic tectonics of New Zealand and the Southwest Pacific, *Earth planet. Sci. Lett.,* **361,** 460–468.

Russell, J.B., Eilon, Z. & Mosher, S.G., 2019. Obsrange: a new tool for the precise remote location of ocean-bottom seismometers, *Seismol. Res. Lett.,* **90**(4), 1627–1641.

Ryan, W. *et al.*, 2009. Global multi-resolution topography synthesis, *Geochem. Geophys. Geosyst.,* **10**(3), doi:10.1029/2008GC002332.

Saffer, D.M. & Bekins, B.A., 2002. Hydrologic controls on the morphology and mechanics of accretionary wedges, *Geology,* **30**(3), 271–274.

Saffer, D.M. & Bekins, B.A., 2006. An evaluation of factors influencing pore pressure in accretionary complexes: Implications for taper angle and wedge mechanics, *J. geophys. Res.,* **111**(4), 1–21.

Saffer, D.M. & Tobin, H.J., 2011. Hydrogeology and mechanics of subduction zone forearcs: fluid flow and pore pressure, *Ann. Rev. Earth planet. Sci.,* **39**(1), 157–186.

Saffer, D.M. & Wallace, L.M., 2015. The frictional, hydrologic, metamorphic and thermal habitat of shallow slow earthquakes, *Nat. Geosci.,* **8,** 594–600.

Salem, H.S. & Chilingarian, G.V., 1999. The cementation factor of Archie's equation for shaly sandstone reservoirs, *J. Petrol. Sci. Eng.,* **23**(2), 83–93.

Savage, H.M. *et al.*, 2021. Asymmetric brittle deformation at the Papaku Fault, Hikurangi Subduction Margin, NZ, IODP Expedition 375, *Geochem. Geophys. Geosyst.,* **22**(8), 1–11.

Scholl, D.W., Kirby, S.H., von Huene, R., Ryan, H., Wells, R.E. & Geist, E.L., 2015. Great (?Mw8.0) megathrust earthquakes and the subduction of excess sediment and bathymetrically smooth seafloor, *Geosphere,* **11**(2), 236–265.

Schwalenberg, K., Wood, W., Pecher, I., Hamdan, L., Henrys, S., Jegen, M. & Coffin, R., 2010. Preliminary interpretation of electromagnetic, heat flow, seismic, and geochemical data for gas hydrate distribution across the Porangahau Ridge, New Zealand, *Mar. Geol.,* **272**(1–4), 89–98.

Schwalenberg, K., Rippe, D., Koch, S. & Scholl, C., 2017. Marine-controlled source electromagnetic study of methane seeps and gas hydrates at Opouawe Bank, Hikurangi Margin, New Zealand, *J. geophys. Res.,* **122,** 3334–3350.

Screaton, E., Saffer, D., Henry, P. & Hunze, S., 2002. Porosity loss within the underthrust sediments of the Nankai accretionary complex: implications for overpressures, *Geology,* **30**(1), 19–22.

Seely, D.R., 1977. The significance of landward vergence and oblique structural trends on trench inner slopes, *Island Arcs, Deep Sea Trenches and Back-Arc Basins,* Vol. **1,** pp. 187–198, eds Talwini, M. & Pitman, W.C., American Geophysical Union.

Sen, P. & Goode, P., 1992. Influence of temperature on electrical conductivity on shaly sands, *Geophysics,* **57**(1), 89–96.

Shaddox, H.R. & Schwartz, S.Y., 2019. Subducted seamount diverts shallow slow slip to the forearc of the northern Hikurangi subduction zone, New Zealand, *Geology,* **47**(5), 415–418.

Sun, T., Ellis, S. & Saffer, D., 2020a. Coupled evolution of deformation, pore fluid pressure, and fluid flow in shallow subduction forearcs, *J. geophys. Res.,* **125**(3), 1–26.

Sun, T., Saffer, D. & Ellis, S., 2020b. Mechanical and hydrological effects of seamount subduction on megathrust stress and slip, *Nat. Geosci.,* **13,** 249–255.

Swift, C.M., 1967. A magnetotelluric investigation of an electrical conductivity anomaly in the southwestern United States, *PhD thesis*, Massachusetts Institute of Technology.

Tobin, H.J., Moore, J.C., MacKay, M.E., Orange, D.L. & Kulm, L.D., 1993. Fluid flow along a strike-slip fault at the toe of the Oregon accretionary prism: implications for the geometry of frontal accretion, *Bull. Geol. Soc. Am.,* **105**(5), 569–582.

Turco, F., Crutchley, G.J., Gorman, A.R., Mountjoy, J.J., Hillman, J.I. & Woelz, S., 2020. Seismic velocity and reflectivity analysis of concentrated gas hydrate deposits on the southern Hikurangi Margin (New Zealand), *Mar. Petrol. Geol.,* **120,** doi:10.1016/j.marpetgeo.2020.104572.

van Rijsingen, E., Funiciello, F., Corbi, F. & Lallemand, S., 2019. Rough subducting seafloor reduces interseismic coupling and mega-earthquake occurrence: insights from analogue models, *Geophys. Res. Lett.,* **46,** 3124–3132.

Wallace, L.M., 2020. Slow slip events in New Zealand, *Ann. Rev. Earth planet. Sci.,* **48**(1), 175–203.

Wallace, L.M., Beavan, J., McCaffrey, R. & Darby, D., 2004. Subduction zone coupling and tectonic block rotations in the North Island, New Zealand, *J. geophys. Res.,* **109**(12), 1–21.

Wallace, L.M. *et al.*, 2009. Characterizing the seismogenic zone of a major plate boundary subduction thrust: Hikurangi Margin, New Zealand, *Geochem. Geophys. Geosyst.,* **10**(10), doi:10.1029/2009GC002610.

Wallace, L.M., Webb, S.C., Ito, Y., Mochizuki, K., Hino, R., Henrys, S., Schwartz, S.Y. & Sheehan, A., 2016. Slow slip near the trench at the Hikurangi subduction zone, New Zealand, *Science,* **352**(6286), 701–704.

Wang, C.-Y., Hwang, W.-T. & Cochrane, G.R., 1994. Tectonic dewatering and mechanics of protothrust zones: example from the Cascadia accretionary margin, *J. geophys. Res.,* **99**(B10), 20 043–20 050.

Wang, H., Crutchley, G.J. & Stern, T., 2017. Gas hydrate formation in compressional, extensional and un-faulted structural settings – examples from New Zealand's Hikurangi margin, *Mar. Petrol. Geol.,* **88,** 69–80.

Wang, K. & Bilek, S.L., 2014. Invited review paper: fault creep caused by subduction of rough seafloor relief, *Tectonophysics,* **610,** 1–24.

Warren-Smith, E. *et al.*, 2019. Episodic stress and fluid pressure cycling in subducting oceanic crust during slow slip, *Nat. Geosci.,* **12,** 475–481.

Watson, S.J. *et al.*, 2020. Focused fluid seepage related to variations in accretionary wedge structure, Hikurangi Margin, New Zealand, *Geology,* **48**(1), 56–61.

Weitemeyer, K.A., Constable, S.C., Key, K.W. & Behrens, J.P., 2006. First results from a marine controlled-source electromagnetic survey to detect gas hydrates offshore Oregon, *Geophys. Res. Lett.,* **33**(3), 1–4.

Weitemeyer, K.A., Constable, S. & Trehu, A., 2011. A marine electromagnetic survey to detect gas hydrate at Hydrate, *Geophys. J. Int.,* **187,** 45–62.

Wood, R. & Davy, B., 1994. The Hikurangi Plateau, *Mar. Geol.,* **118**(1–2), 153–173.